THE GEOLOGICAL SOCIETY OF AMERICA®

Characterizing the potential of wind-blown lithium sediments: A case study from Devonian evaporites of the Western Canada Sedimentary Basin

Cody N. Lazowski[1,†], Scott Melnyk[1], Daniela Gutierrez-Rueda[1], Jiuyuan Wang[2], Lidya G. Tarhan[3], Tyler E. Hauck[4], Daniel S. Alessi[1], Kurt O. Konhauser[1], and Murray K. Gingras[1]

[1]*Department of Earth and Atmospheric Sciences, University of Alberta, Edmonton, Alberta T6G 2E3, Canada*
[2]*Key Laboratory of Orogenic Belts and Crustal Evolution, MOE, School of Earth and Space Sciences, Peking University, Beijing 100871, China*
[3]*Department of Earth and Planetary Sciences, Yale University, New Haven, Connecticut 06511, USA*
[4]*Alberta Geological Survey/Alberta Energy Regulator, Edmonton, Alberta T6B 2X3, Canada*

ABSTRACT

Elevated lithium (Li) within the formational waters of deep sedimentary basins continues to garner attention as a widespread addition to global Li resources. However, the nature of Li emplacement remains understudied. Here we document elevated Li in Devonian evaporites of the Western Canada Sedimentary Basin and reconstruct the processes that led to their enrichment. Our results show bulk Li concentrations ranging from 49.4 ppm to 284 ppm. Contrary to previous speculation that Li is hosted within evaporitic minerals, our findings indicate that it is instead within aggregate grains of clay-sized particles composed of micas and clay minerals. The Li-bearing grains range from subangular to rounded, displaying a bimodal distribution with particle fractions of either medium- to coarse-grained silt or very fine sand. The individual particles average 304 ppm Li and attain concentrations as high as 394 ppm. Previous work has shown that Li was weathered from Precambrian basement and transported into the basin via fluvial discharge; however, no attempt has been made to characterize the distribution of these sediments by wind-borne processes. Thin sections reveal that these aggregate grains are widespread and that they dominantly occur in supratidal sediments, waning in abundance into lower intertidal deposits. Based on the particle distribution and several other lines of evidence, we suggest that these Li-rich detritals were deposited by wind-borne processes, and the results herein are the first to characterize the potential of wind-blown Li sediments. Given the extent of enrichment in these evaporites, we propose that aeolian processes play an important yet underappreciated role in transporting and accumulating Li-rich sediments. As alternative Li resources continue emerging, these findings highlight the potential of wind transport and provide a predictive framework for the paleogeographic distribution of Li-rich strata and their associations with Li-enriched brines.

INTRODUCTION

Lithium is a critical element in the development of renewable energy technologies, in large part driven by the adoption of Li-ion batteries in electric vehicles and consumer electronics (Ambrose and Kendall, 2019). From 2008 to 2018, the production of energy storage technologies increased eightfold, and today, batteries account for over 80% of global Li end use (Buyung Agusdinata et al., 2018; USGS, 2023). By 2020, this resulted in the production of >11 million electric vehicles, and with continued demand, forecasts suggest that >140 million electric vehicles will be produced by 2030 (Buyung Agusdinata et al., 2018; IEA, 2021). Current Li resources total an estimated 98 million tons and consist of granitic pegmatites rich in Li-bearing minerals such as spodumene and lepidolite, Li-clays, and dissolved Li in surface and subsurface continental brines (Bowell et al., 2020; USGS, 2023). Granitic pegmatites are widespread and highly variable in their composition, with Li-bearing pegmatites representing a single family termed LCT (Li-Cs-Ta) pegmatites (Černý and Ercit, 2005). LCT pegmatites form by partial melting of middle to upper crust protoliths where rare elements mobilize into the silicate melt and are further concentrated through fractional crystallization during their ascent into the shallow crust (Černý et al., 2005). At the very late stages of crystallization, the remaining melt is water saturated and highly enriched in rare elements, leading to the crystallization of Li-bearing minerals (Deveaud et al., 2015). Although they are rare, LCT pegmatites can be high grade (e.g., Greenbushes pegmatite, Australia ~2.6 wt% Li_2O) and account for ~50% of current Li production (Bowell et al., 2020; USGS, 2023).

Clay deposits have garnered attention as a resource of the near future (Bowell et al., 2020). They are broadly defined as anomalous accumulations of Li in clay materials, which have a genetic or spatial relationship to rhyolitic volcanics or felsic igneous rocks (Evans, 2014). Li-clays include those in which Li is structurally bound (i.e., hectorite) or where Li is sorbed to the surfaces of clay minerals or within interlayers (i.e., illite or muscovite; Benson et al., 2017; Bowell et al., 2020). Although the origins of these deposits are still under debate, they are interpreted to form through the weathering of Li from nearby volcanic ash and igneous rocks or through high temperature water-rock interactions transporting Li into a closed lacustrine basin where Li may be adsorbed to non-hectorite clays or bound in hectorite through subsequent alteration (Hofstra et al., 2013; Benson et al., 2017; Coffey et al., 2021; Gagnon et al., 2023). The McDermitt caldera in Nevada, USA, is the best-known clay deposit, estimated to be the world's fifth largest in situ Li resource (Castor and Henry, 2020). Here, Li is primarily hosted within a variably mixed smectite-illite claystone with average concentrations ranging from ~1500 ppm to 3000 ppm (Castor and Henry, 2020).

Continental brines constitute the largest deposits, estimated to host nearly 60% of global Li resources and account for ~49% of global

Cody N. Lazowski https://orcid.org/0000-0002-1936-1311
[†]lazowski@ualberta.ca

GSA Bulletin; November/December 2025; v. 137; no. 11/12; p. 4955–4970; https://doi.org/10.1130/B38104.1.
Published online 9 June 2025

production (USGS, 2023). They are interpreted to form where Li is mobilized by hydrothermal fluids or the weathering of nearby igneous rocks and accumulates in an intracontinental evaporitic basin or its subsurface waters (Bradley et al., 2013). All economically developed brines are of Quaternary age and occur in regions with an arid climate, closed basin containing a playa or salar (salt pan), with nearby geothermal activity or igneous source rocks (Bradley et al., 2013). The largest brine deposits are found in the hyper-arid salt flats of Chile, Bolivia, and Argentina, where concentrations regularly exceed 1000 mg/L, and in some localities, reach as high as 5000 mg/L (Munk et al., 2018).

Despite the identification of numerous Li resources worldwide, current supply remains limited to hard rock mining and evaporative brine extraction—both of which face geopolitical and socio-environmental challenges (Flexer et al., 2018; Buyung Agusdinata et al., 2018; Vera et al., 2023). Consequently, governments and manufacturers have prioritized the evaluation of alternative resources to establish a diversified and reliable supply chain (Benson et al., 2017; USGS, 2023; Vera et al., 2023). In addition to clay deposits, Li within deep continental brines has been recognized as a future resource. Groundwater hosted within ancient sedimentary basins has long been recognized for its high concentrations of dissolved metals and global distributions (Kharaka and Hanor, 2003). Li was first identified in the Smackover Formation, Arkansas, USA, where concentrations nearing 700 mg/L were detected (Collins, 1976). Since then, Li has been identified in 48 sedimentary basins across six continents, with concentrations reaching up to 1800 mg/L (Dugamin et al., 2021). Although deep formational waters are generally low-grade, their vast volumes make them an attractive target for secondary evaluation, particularly as they are already extracted at byproducts of oil, gas, and low enthalpy geothermal operations worldwide (Maloney and Yoxtheimer, 2012; Lund and Toth, 2021).

Although Li-rich deep formational brines have been widely recognized, their sources and mechanisms of enrichment remain poorly understood. Most efforts to reconstruct these brines suggest that they developed through a combination of late-stage seawater evaporation, meteoric water mixing, hydrothermal influx, and complex water-rock interactions (Connolly et al., 1990a, 1990b; Wilson and Long, 1993; Tesmer et al., 2007; Sanjuan et al., 2022). Although this approach may provide valuable insights into groundwater chemistry, it is often constrained by the limited availability of rock data, relying on generalized models that lack direct geologic context.

This is especially true in the Western Canada Sedimentary Basin, where brines with Li concentrations reaching over 115 mg/L are recognized in the Devonian aged Beaverhill Lake, Woodbend, and Wabamun Groups of west-central Alberta, and brines from the Devonian aged Duperow Formation of western Saskatchewan show concentrations up to 190 mg/L (Hitchon et al., 1993; Eccles and Berhane, 2011; Jensen, 2020). Previous investigations into brines along the western portion of the Alberta basin have noted a correlation between increased radiogenic $^{87}Sr/^{86}Sr$ levels and elevated Li (Eccles and Berhane, 2011). They suggest Li enrichment resulted from a post-depositional influx of basement-derived hydrothermal fluids, which migrated along the overlying siliciclastics and upward into carbonate units (Eccles and Berhane, 2011; Huff, 2016). Eastward into central Alberta, a more recent analysis of stable hydrogen and oxygen isotopes suggests these brines formed through evaporation-concentration of seawater and that the Li was later emplaced by the dissolution of in situ Li-bearing evaporitic minerals (Huff, 2016, 2019). Although these hypotheses are compelling, no direct evidence of Li-rich evaporites or hydrothermal transport has been presented.

To test the hypothesis of hydrothermal emplacement, Lazowski et al. (2025) examined the Precambrian basement and its overlying siliciclastic and carbonate units. These units were examined both within and outside of the fault zone proposed as a migration pathway for exhumed hydrothermal fluids, and these rocks were analyzed for their Li concentration and isotopic content to determine (1) whether Li exists within these sediments and (2) if Li emplacement can be attributed to hydrothermal processes (Lazowski et al., 2025). They found that the distribution of Li concentrations (0.4–167.3 ppm) and δ^7Li values (1.5‰–23.5‰) are lithofacies dependent and directly related to weathering and the extent of secondary mineral formation (Lazowski et al., 2025). Their results demonstrate an ancient weathering profile from which Li is derived from crystalline basement and retained in paleosols or transported into the basin via fluvial drainage syndepositional to development of the Alberta basin (Lazowski et al., 2025). Moreover, they suggest that large-scale evaporation of the basin concurrent with the continental delivery of Li contributed to the enhanced Li concentrations previously suggested in Devonian seawater of the Western Canada Sedimentary Basin (Lazowski et al., 2025). Their efforts established a framework for understanding the genesis of Li in deep-time contexts and highlights the crucial role of weathering processes in mobilizing and transporting Li at Earth's surface (Lazowski et al., 2025).

Here, we examine evaporitic rocks from the Devonian aged Beaverhill Lake Group for their Li concentrations. We report elevated Li in evaporites of the Fort Vermilion Formation, with bulk concentrations up to 284 ppm, and demonstrate that the Li in these evaporites is not hosted within late-stage evaporitic minerals (i.e., carnallite) as previously suggested, but rather within silt–very fine sand sized aggregate grains composed of micas, feldspars, and clays. Lithofacies analyses of these deposits show that like modern Li resources, these strata were deposited in an evaporative, restricted environment proximal to the actively weathering crystalline rocks described by Lazowski et al. (2025). We link these Li-bearing aggregate grains to previously described paleosols formed from the crystalline rocks, and crucially, we demonstrate that these aggregate grains were emplaced through aeolian processes and that their distribution and preservation potential is facies dependent. Our findings characterize the potential of wind-driven Li-bearing sediments originating from exposed crystalline rocks and leading to its accumulation in a marine evaporitic basin-margin.

Aeolian sediment generation and transport are widely recognized as fundamental Earth systems processes (Harrison et al., 2001; McGee et al., 2016). Present-day rates of aeolian sediment mobilization are estimated to range from ~1.0 gigatons/yr to 3.0 gigatons/yr (Cakmur et al., 2006; Tanaka and Chiba, 2006). At these rates, aeolian sediments influence climate by scattering and absorbing solar radiation and impact oceanic biogeochemistry by delivering micronutrients essential for enhancing primary productivity and CO_2 uptake (Kohfeld and Harrison., 2001; Maher et al., 2010; McGee et al., 2016). Although sediment and ice cores have recorded large, systematic variations in the paleo-dust record, aeolian transport has remained a vital mechanism for redistributing weathered sediments and their associated trace metals across Earth's surface (Maher et al., 2010). In the case of Li, loess has been previously recognized as a possible source for evaporitic brines (Bradley et al., 2013); however, no substantive attempts have been made to quantify its potential. Considering the substantial annual flux of aeolian sediment transport and Li concentrations within individual grains—reaching up to 394 ppm—our results suggest that aeolian processes play a more significant role in the transport of Li-rich sediments than previously recognized. Moreover, the paleogeographic distribution of these sediments may be predictable. These findings underscore the importance of developing a robust geological framework to better characterize Li sources and distribution within deep sedimentary basins.

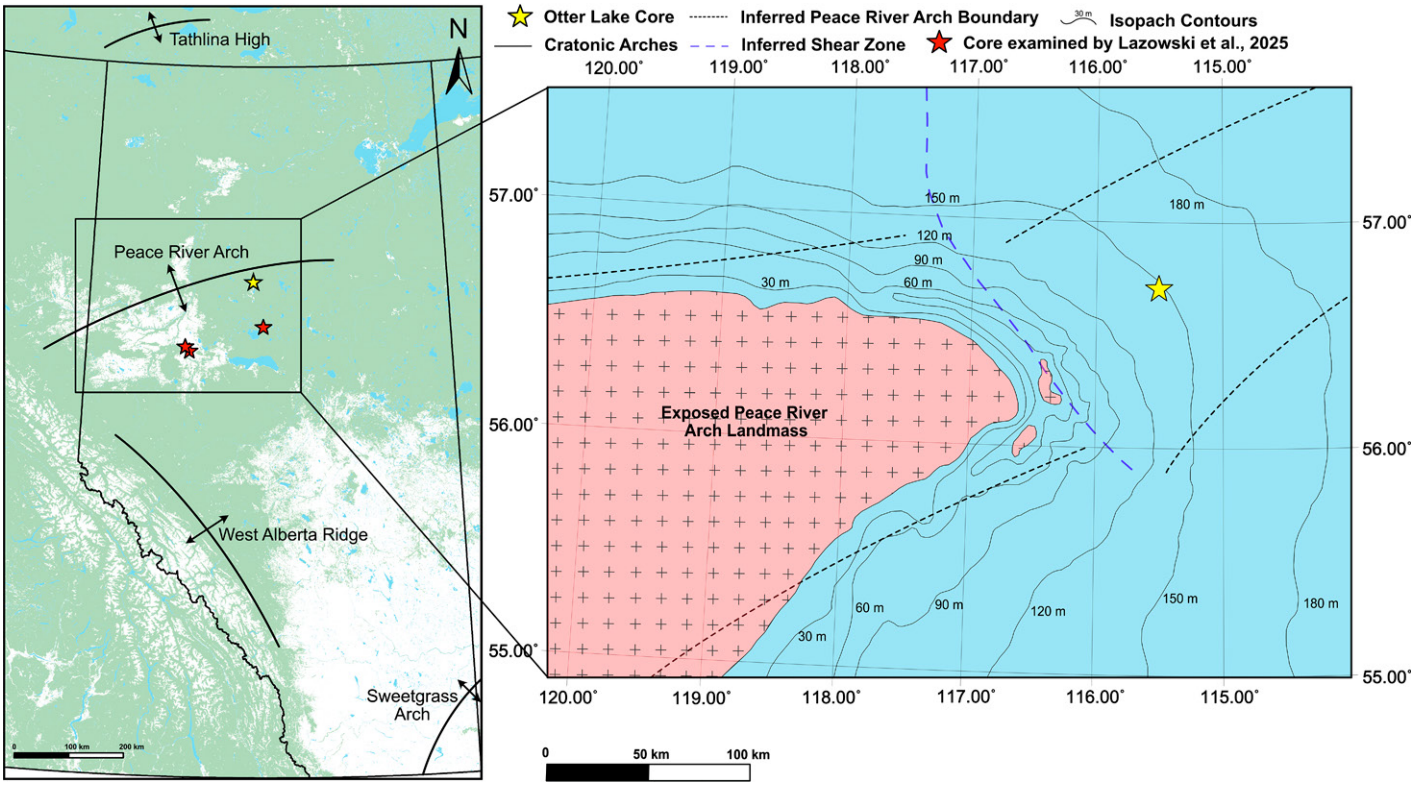

Figure 1. (Left) Sample location map outlining the major structural uplifts that influenced sedimentation in the Western Canada Sedimentary Basin throughout the Devonian (modified from O'Connell et al., 1990). (Top Right) Inset map of the Peace River Arch during the Middle-Upper Frasnian; the blue area represents an isopach of the total thickness of Beaverhill Lake Group sediments and dashed black lines represent the inferred limits of the Arch (modified from Trotter and Hein, 1988 and Keith, 1990). The yellow star indicates the location of core used in this study, and the red stars indicate the location of core analyzed by Lazowski et al. (2025).

Geologic Setting of the Western Canada Sedimentary Basin

Sedimentary rocks along the western edge of the North American Craton are primarily attributed to continental rifting and the initiation of a passive margin in the late Precambrian between ca. 600 Ma and 555 Ma (Bond and Kominz, 1984). This resulted in the development of a passive Paleozoic margin, of which the earliest deposits record a far-reaching transgressive onlap of the craton (Bond and Kominz, 1984). The extent of transgression is attributed to a period of tectonic subsidence due to lithospheric cooling and sediment loading, along with a simultaneous sea-level rise of the Sauk Sequence (Porter et al., 1982; Bond and Kominz, 1984). Deposits of the Sauk Sequence consist of diachronous sandstones ranging in age from Early Cambrian to Ordovician and extend along the entire western flank of the craton (Porter et al., 1982). These sandstones represent the first sediments of the Western Canada Sedimentary Basin. Relative sea level continued to rise through the Middle–Late Cambrian, where the basal sandstones were overlain by transgressive cycles of siltstones and shales. A subsequent lowering of sea level then led to grading into shallow water carbonates along the western margin of the basin (Aitken, 1971). Beyond early subsidence of the westernmost margin, the North American Craton remained a stable platform for the development of shallow-marine deposits throughout the remainder of the Cambrian and into the Early Ordovician (Porter et al., 1982).

Following the Sauk Sequence, little strata were preserved near the western margin of North America until the Middle Devonian, when a series of arches and ridges extensively influenced the distribution, thickness, and character of Western Canada Sedimentary Basin sediments (Fig. 1; Cant, 1988; Porter et al., 1982). Three major structures have been recognized: the Peace River Arch (PRA), the West Alberta Ridge, and the Tathlina High (O'Connell et al., 1990). The PRA is the largest of these features, represented by an east-northeast–trending cratonic high that extends ~700 km from northeastern British Columbia into northwestern Alberta (Cant, 1988). The arch is ~140 km wide with an asymmetrical shape, dipping more steeply to the north and gently to the south (Trotter, 1989; O'Connell et al., 1990). At its peak near the British Columbia–Alberta border, it rose 800–1000 m above regional basement elevation and 400–500 m above regional elevation near its eastern extent (Cant, 1988). The West Alberta Ridge lies south of the PRA and parallels the passive margin, forming a south–southeast continuation of the PRA landmass (Moore, 1989). To the north, the Tathlina High paralleled the PRA, forming a northeast-trending uplift throughout northwest Alberta and the District of Mackenzie (Moore, 1989). Together, these arches enclosed topographic depressions to the north and south of the PRA, which shed sediment into these basins during renewed cycles of transgression and regression during the Cambrian–Late Devonian (Porter et al., 1982; Trotter, 1989).

Reactivation of the basement throughout the early Phanerozoic resulted in normal faulting along the axis of the Arch, and by the Middle Devonian, the PRA became riddled with high-relief horsts and grabens (Balshaw, 2010; Sikaboyni and Rodgers, 1959). Although the origins of the PRA are still poorly understood, numerous authors have contributed to understanding the history of its development, and theories for

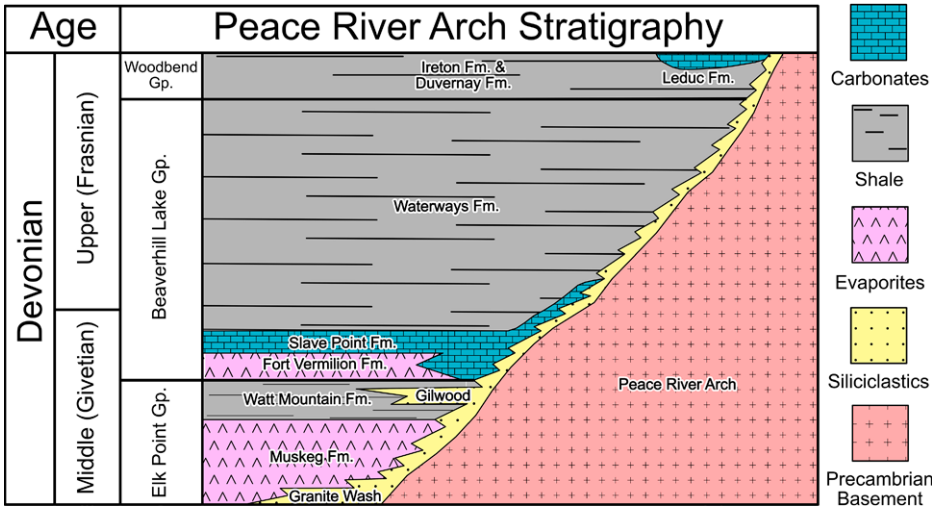

Figure 2. Schematic of the Middle Devonian stratigraphy around the Peace River Arch (PRA). An overall transgression of the PRA was punctuated by several regressive events, the most prominent being the Gilwood Member. Following a period of regression, sea level remained low, allowing for the development of evaporite and carbonate sequences along the flanks of the PRA.

the upward movement of Precambrian rock include doming due to a mantle hotspot (Burwash and Krupicka, 1970; Stelck, 1975; Stelck et al., 1978), a failed Paleozoic rift system (Cant, 1988), flexural uplift of the basement (Beaumont et al., 1993), and transform faulting along a mid-ocean ridge (O'Connell et al., 1990; McMechan, 1990). Despite all of the basement faulting throughout its complex history, there is no known hydrothermal alteration of the basement-derived siliciclastics that infill the grabens or reside along its flanks; however, Lazowski et al. (2025) have shown a link between K-metasomatism and Li enrichment in the Precambrian basement.

Regional Geology of the Peace River Arch

The earliest deposits to drape the PRA are siliciclastics of the Granite Wash, which are sediments derived from, and unconformably overlying, the Precambrian rocks that make up the PRA (Fig. 2; Trotter and Hein, 1988). They are weathered from basement rocks of the PRA and are present on the crest of the high-relief structure, filling grabens and other paleotopographic lows, and within the shallow marine basins flanking the Arch (Dec et al., 1996). They characterize a wide range of depositional environments, including alluvial fan, braided river, estuary, and shallow marine facies (Trotter and Hein, 1988). The Granite Wash is highly diachronous, and its age is only known where it is found interbedded with Middle–Upper Devonian strata of the Elk Point and Beaverhill Lake groups (Cant, 1988).

Restricted sea-water circulation during deposition of the Elk Point Group led to an accumulation of evaporites, carbonates, and shallow marine clastics that onlap the flanks of the PRA and interfinger with stratigraphically equivalent, backstepping Granite Wash sediments (Hauck and Grobe, 2020). Transgression of the PRA was punctuated by several regressive events during the Devonian in which arch-derived siliciclastics prograded into the basin (e.g., Balshaw, 2010). The Gilwood Member is the most extensive of these, comprising arkosic sandstones that represent a fluvial-deltaic transitional sequence that developed along the coastal plain of the Arch (Jansa and Fischbuch, 1974; Shawa, 1969).

Following deposition of the Elk Point Group, the PRA remained an emergent, topographic high throughout the Beaverhill Lake Group, of which the earliest deposits comprise the Fort Vermilion and Slave Point Formations (Fig. 1; Keith, 1990). Fort Vermilion strata consist of nodular to massive anhydrites interbedded with dolomitic muds and laminated anhydrite (Hauck, 2014). These evaporitic sequences are believed to be the result of a brief period of sea level stand-still or slight regression following Elk Point deposition and prior to the overall transgressive phase that dominated the Middle–Late Devonian (Fig. 3; Jansa and Fischbuch, 1974; Keith, 1990). They conformably overly shales and terrigenous clastics of the Watt Mountain Formation and formed along the extensive coastal plain of Gilwood member siliciclastics (Jansa and Fischbuch, 1974). These evaporites are characterized as supratidal, intertidal, and lagoon deposits (Jansa and Fischbuch, 1974). Fort Vermilion strata extend up to 80 km wide around the PRA, pinching out on the Arch and thickening into the basin to ~25 m (Fig. 3; Jansa and Fischbuch, 1974; Keith, 1990).

Relative sea level continued rising, and the Fort Vermilion Formation was conformably overlain by platform carbonates of the Slave Point Formation (Hauck, 2014). These carbonates are dominated by a fossiliferous lime mudstone reaching up to ~12 m in thickness away from the PRA (Keith, 1990). Along the margins of the Arch, the Slave Point Formation extends beyond the underlying strata, onlapping Granite Wash sediments (O'Connell et al., 1990). Continued sea level rise led to the deposition of open marine calcareous shales and dark gray nodular limestones, which make up the overlying Waterways Formation (Jansa and Fischbuch, 1974). Detailed maps outlining the distribution of Devonian stratigraphy are provided by Lazowski et al. (2025).

This study examines, in the framework of the development of the PRA, the Li content within rocks from a section of core from north-central Alberta (UWI location 01-01-089-10-W5), including the Fort Vermilion, Slave Point, and Waterways formations (Fig. 1). These strata were deposited proximal to the PRA, where a fluvial-deltaic system draining the crystalline basement has been shown to accumulate and transport Li into the Alberta Basin (Lazowski et al., 2025).

METHODS

A detailed description of the methods used in this study are provided in section 1 of the Supplemental Material.[1] Briefly, they include core logging, sample collection, aqua regia digestion and element analysis, X-ray diffraction, petrographic microscopy, and laser ablation–inductively coupled plasma–mass spectrometry (LA-ICP-MS). Slabbed core from UWI location 01-01-089-10-W5 was logged and sampled at the core facility in the University of Alberta, Edmonton, Alberta, Canada. Bulk analysis of Li and major element concentrations was conducted by partial digestion of each sample using aqua regia. Samples were analyzed on an Agilent 8800 Triple Quadrupole ICP-MS (inductively coupled plasma–mass spectrometer) in the Geobiology Laboratory at the University of Alberta. Powder X-ray diffraction (XRD) was performed in the X-ray Diffraction Laboratory at the University of Alberta. Following the identification of Li-rich strata and establishment of its relationship

[1]Supplemental Material. Section 1 details core logging and analytical methods and section 2 provides full lithofacies descriptions. Please visit https://doi.org/10.1130/GSAB.S.28934234 to access the supplemental material; contact editing@geosociety.org with any questions.

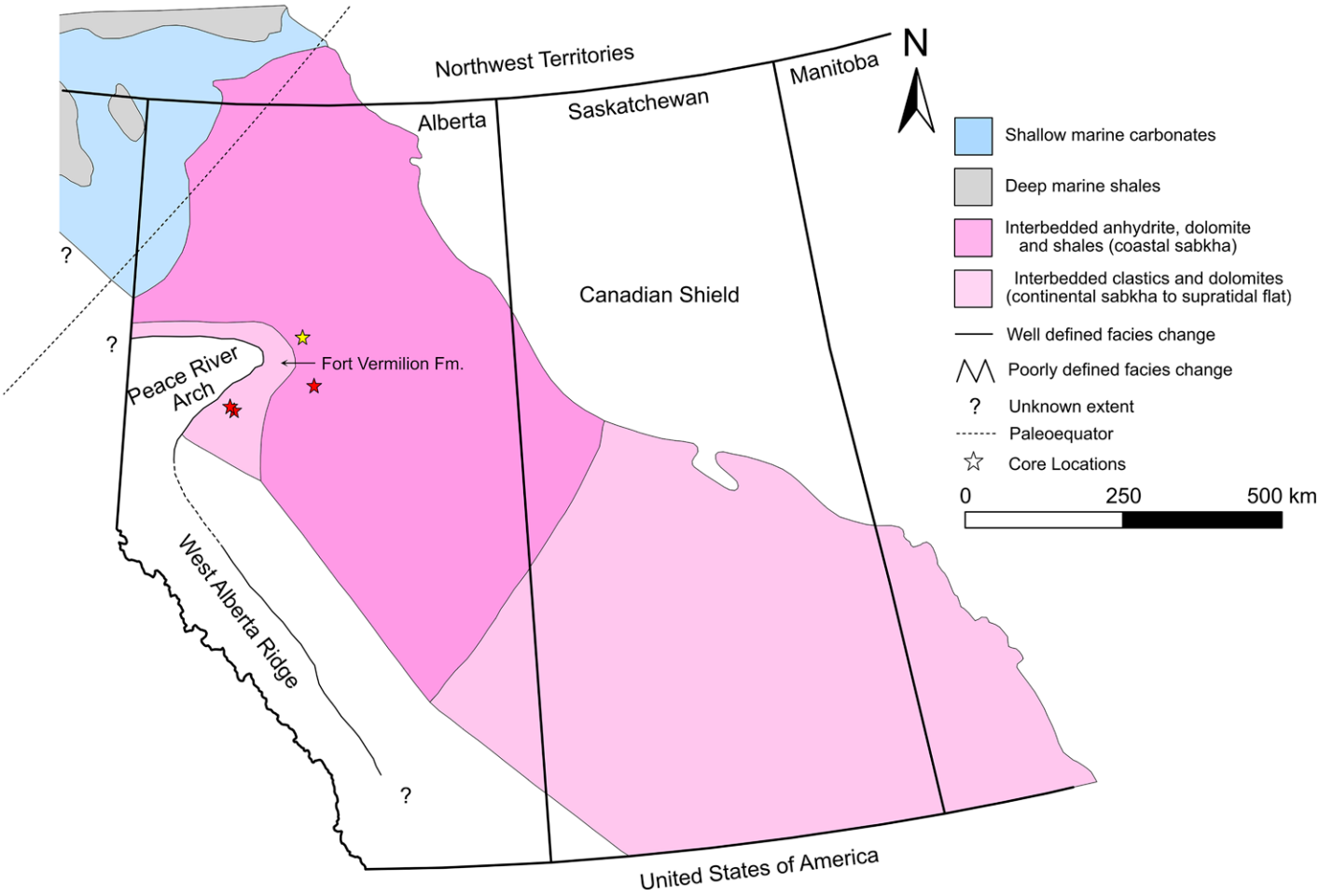

Figure 3. Distribution of the Fort Vermilion Formation and its equivalents during a brief period of sea level standstill or slight regression in the Middle Devonian (modified from Meijer Drees, 1994). The yellow star indicates the location of core used in this study and the red stars indicate the location of core examined by Lazowski et al. (2025).

with mineralogy and major elements, paired thin (30 μm thick) and thick (100 μm thick) sections were prepared in the University of Alberta's thin section laboratory. The thin sections were described using a transmitted light petrographic microscope, and these descriptions guided in situ LA-ICP-MS measurements for detailed spot analysis (Li, Al, Fe, Mg, K, Ca). LA-ICP-MS analysis was conducted at the Yale Metal Geochemistry and Geochronology Center, Yale University, New Haven, Connecticut, USA, using an ESL NWR193 laser ablation system coupled with a ThermoFisher iCAP-Q ICP-MS. Spot analyses were bracketed with repeat measurements of the reference material U.S. National Institute of Standards and Technology Standard Reference Materials (NIST)-610. Data were processed using Iolite software developed by Paton et al., 2011. Error on the concentrations of all elements measured within 0.2% of the accepted NIST-610 value.

Geological Facies and Depositional Setting

Figure 4 outlines a summary of each facies including the core expression, lithologic characteristics, mineralogy, and range of bulk Li concentrations. Section 2 of the Supplemental Material provides full descriptions of each lithofacies and interpretations of their depositional setting. Figure 5 outlines photographs of the full core, including sample locations for reference.

Core Interpretation

The existence of calcareous laminae in Facies 1 implies that this facies was deposited by suspension settling in a tranquil, submarine setting (such as a lagoon or sheltered bay margin) with hydraulic continuity with the larger basin, limiting evaporite mineral formation (Warren and Kendall., 1985). Lamina sets are thicker and more calcareous near the bottom of the facies, grading upward into thinner, dolomitic packages. Anhydrite stringers and nodules are more common as dolomitic content increases. The thinning of lamina sets and a shift from dominantly calcareous to dolomitic mudstones suggests that water depth subsequently decreased into a more restricted marine environment where shallower water limited the development of lamina sets and increased evaporation promoted the precipitation of primary evaporitic minerals (Schreiber and El Tabakh, 2000). This facies is interpreted to have formed in a restricted lagoonal setting.

Facies 2 is sharp based and marks a shift to massive dolomitic mudstones containing mm-scale microbial laminae intercalated with laminated and occasionally convolute anhydrite beds. The disappearance of calcite, frequent precipitation of gypsum (now anhydrite), and prevalence of dolomitic mudstone suggest deposition within a more restricted shallow marine/evaporative environment than Facies 1, where the produc-

Facies Name	Massive to laminated calcareous and dolomitic mudstone	Massive and microbial laminated to brecciated dolomitic mudstone interbedded with laminated anhydrite	Laminated to enterolithic dolomite, anhydrite and halite	Planar laminated anhydrite and dolomite interbedded with convolute dolomitic mudstone	Microbially laminated calcareous mudstone	Massive to microbially laminated nodular calcareous mudstone	Nodular wackestone interbedded with calcareous mudstone
Core Expression		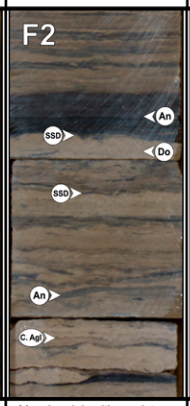		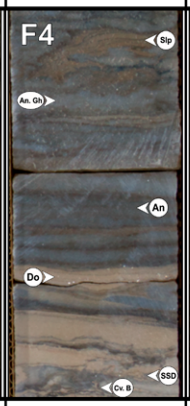	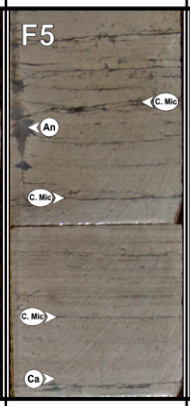		
Lithologic Description	Massive to laminated calcareous and dolomitic mudstones. Massive-appearing beds often contain mm-scale anhydrite nodules appearing brecciated. Interbedded with planar to low angle laminated anhydrite beds. Lamina sets range 0.5 - 2 cm in thickness and tend to thin where dolomite content increases. Thin stringers of anhydrite occur throughout, but tend to increase in abundance with dolomitic-rich beds..	Massive dolomitic mudstone containing microbial laminae interbedded with laminated and occasionally convolute bedded anhydrite. The massive dolomitic beds contain disseminated anhydrite throughout, and less commonly show displacive anhydrite growth. Microbial laminations occur throughout in thin lamina sets. Soft sediment deformation and slumping can be found throughout the laminated anhydrite.	Planar laminated dolomite and anhydrite interbedded with enterolithic to nodular anhydrite. Lamina sets range 1-4 cm in thickness and consist of roughly equal proportions of dolomite and anhydrite. Enterolithic and nodular anhydrite beds range 2-10 cm in thickness and occasionally show relict planar bedding. Anhydrite nodules and stringers are sporadically distributed throughout.	Planar to low angle laminated anhydrite and dolomite. Anhydrite lamina sets range 1-10 cm in thickness and sometimes display convolute bedding and slumping. Slumping typically occurs where planar bedding grades into low angle bedding and the proportion of dolomitic mud increases. Laminated intervals are interbedded with massive to nodular anhydrite.	Microbial laminated carbonates, facies 5 marks a sharp mineralogical shift from dolomite to calcite. The microbial laminae commonly include vertically transecting fractures. Smaller fractures tend to be filled with calcareous mudstone, whereas larger fractures (>2 cm) are exclusively anhydrite-filled. Secondary, displacive anhydrite growth is common throughout, where it often destroys any visible laminae.	Massive-appearing to microbially laminated calcareous mudstone. Nearly all laminae are disrupted by nodular limestone, which in some cases dominates entire sections of the facies, leading to a mottled appearance. Sub-spherical to columnar stromatolites are sporadically found throughout. Rare articulated brachiopods can be found within massive beds.	Nodular wackestone interbedded with calcareous mudstone. Secondary calcareous nodules dominate, disrupting nearly all original bedding and leaving majority of the facies with a mottled texture. Brachiopods are common throughout, with disarticulated and fragmented brachiopods typically concentrated within sharp based cm-scale beds.
XRD Mineralogy	Anhydrite, dolomite, quartz, microcline	Dolomite, Mg-bearing calcite, anhydrite, quartz, muscovite	Dolomite, Mg-bearing calcite, anhydrite, muscovite, dickite clinochlore, orthoclase, kaolinite, albite, halite, sylvite, quartz	Anhydrite, dolomite, quartz	N/A	N/A	N/A
Bulk Lithium	57.7 - 59.1 ppm	49.4 - 109.0 ppm	118.0 - 284.0 ppm	Below detection limit (< 0.25 ppm)	Below detection limit (< 0.25 ppm)	Below detection limit (< 0.25 ppm)	Below detection limit (< 0.25 ppm)

Figure 4. Core expression of each of the seven facies, labeled F1 through F7, and including their X-ray diffraction (XRD) mineralogy and bulk Li concentration. Facies are characterized by their lithology, texture, and sedimentary structures in the descriptions provided. An—anhydrite; Ca—calcareous; Do—dolomitic; SSD—soft sediment deformation; C. Mic—microbial laminations; Ent.—enterolithic folding; An. Gh—anhydrite ghost; Slp—slumping; Cv. B—convolute bedding; Ndl—nodular limestone; Bpd—brachiopod.

tion of dolomite is both evaporative and likely microbially induced (Shearman, 1978; Vasconcelos and McKenzie, 1997; Schreiber and El Tabakh, 2000; Petrash et al., 2017). The presence of displacive anhydrite crystals and rare teepee structures supports this interpretation, implying at least periodic subaerial exposure (Warren, 2016). However, these beds occasionally show soft-sediment deformation of the underlying dolomitic units suggesting subaerial exposure was brief, and the water table remained high enough that the muds were always saturated. Up-section, the dolomitic beds become thinner, and the proportion of anhydrite increases, indicative of more frequent periods of exposure. These deposits are interpreted to have formed in a more landward marine setting than Facies 1, somewhere within the upper intertidal to supratidal zone.

Facies 2 gradationally transitions into Facies 3 where the entirety of this facies constitutes mm-scale planar-laminated anhydrite, dolomite, and minor halite, although much of the original structure is overprinted by enterolithic folding and nodular anhydrite. Planar laminae are most common near the base of the facies, with enterolithic folded beds becoming increasingly prevalent up-section and dominating the middle portion of this facies, where rare desiccation cracks occur. Near the top, displacive enterolithic textures becomes less common and planar laminae reappears, until the top of the facies is again sharply overlain by Facies 2. Thinner, more abundant laminae, the disappearance of wavy-crinkly microbial mats, and the appearance of halite suggest Facies 3 formed under more restricted, hypersaline conditions with evaporation reaching at least halite saturation (Warren, 2016). The transition from microbial laminae of Facies 2 into planar laminated anhydrite and dolomitic mudstone, through enterolithic bedding and back into planar laminae over an ~85 cm interval illustrates a typical sabkha sequence, which is subsequently flooded (Shearman, 1978; Schreiber and El Tabakh, 2000).

Facies 4 comprises planar laminated anhydrite and dolomite that are sporadically interbedded with convolute bedded dolomitic mudstone. Near the base of this facies, laminae are regular and do not show any displacive crystal growth, suggesting the water became deep enough for deposition in a low-energy environment through suspension settling, where evaporation near the surface of the water caused the precipitation of mud-sized evaporitic cumulates, which fell through the water column and precipitated as stratified laminates (Kirkland et al., 2000; Warren, 2016). These lamina-sets are sporadically interbedded with sharp-based beds of massive to convolute-laminated dolomitic mudstones, which become more pervasive up section. The convolute bedded dolomitic mudstones commonly show flame structures and ball and pillow soft sediment deformation into the underlying evaporites. This suggests that these beds were rapidly deposited, likely as storm events. Farther up-section, lamina-sets become thinner and are interbedded with thin beds of gypsum "ghosts." These are secondary features that preserve the original texture of gypsum growth by binding muds to the crystal boundaries prior to burial and conversion to anhydrite (Warren and Kendall., 1985). Here, gypsum ghosts show that short, bottom nucleated gypsum crystals grew in isolated interbeds with planar laminates. Altogether,

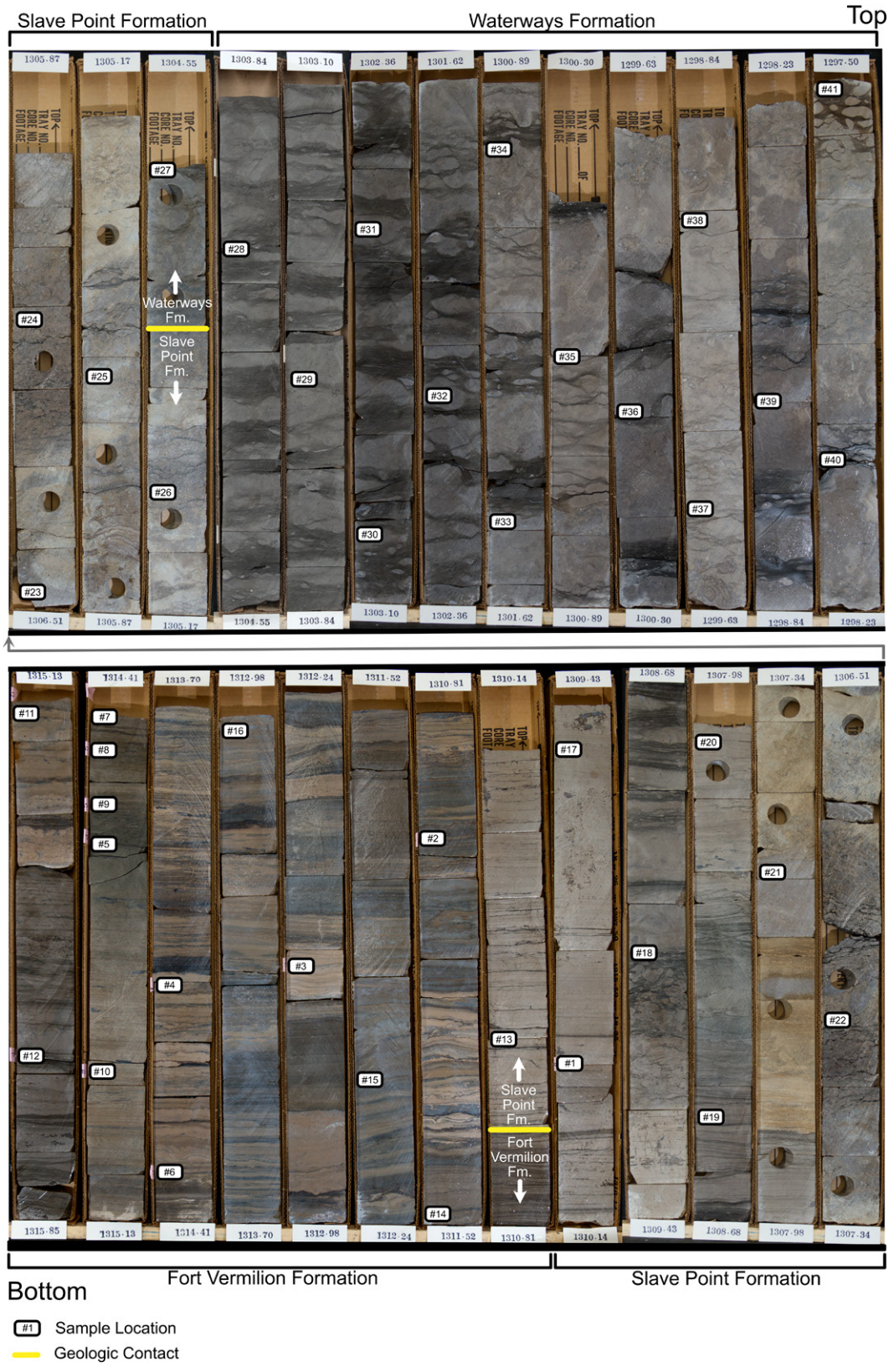

Figure 5. Photographed core in the interval 1297.5–1315.13 m from 01 to 01-089-10-W5. The Fort Vermilion Formation consists of anhydrite and laminated microbial dolomites with occasional enterolithic bedding, anhydrite "ghosts," brecciation, soft-sediment deformation, and otherwise chaotic bedding. The Slave Point Formation consists of microbially laminated calcareous muds that grade upward into massive and laminated carbonates. The Slave Point Formation is overlain by the shaley, nodular, and burrowed carbonates of the Waterways Formation. The base of the core is the bottom left of the photo and the top of the core is in the top right.

these sequences suggest that Facies 4 was first deposited within a deeper water restricted lagoonal environment (but still above storm wave base). However, evaporitic drawdown episodically led to the growth of bottom nucleated gypsum.

Facies 5 marks the lowermost deposits of the Slave Point Formation and a major lithologic shift from primarily dolomite and anhydrite

into calcite. It largely consists of microbial and planar-laminated lime mudstones. Anhydrite nodules are present throughout, although they constitute <10% of the facies. They also crosscut all other primary textures, indicating they are diagenetic. The disappearance of dolomite and introduction of primarily lime mudstones indicates an environmental shift toward less restricted marine conditions. The presence of microbial laminae within low-angle to planar-laminated lime mudstones suggests low-energy deposition within the intertidal zone (Warren and Kendall, 1985).

Facies 5 grades into Facies 6, which is characterized by a massive to microbial-laminated lime mudstone. Nearly all laminae are disrupted by the development of nodular limestone, leaving a mottled texture throughout much of the facies. Sub-spherical to columnar stromatolites are sporadically found throughout, and rare, small articulated brachiopods are present. These suggest Facies 6 was deposited in a relatively open marine, lagoonal environment.

Facies 6 and 7 share a gradational contact. Facies 7 consists of a nodular wackestone with interbedded dark-colored calcareous mudstone. Like Facies 6, nearly all laminae are disrupted by the development of calcareous nodules or burrowing, leaving the entirety of this facies with a mottled texture. Brachiopods are common throughout and range in size from 1 cm to 3 cm. The disappearance of stromatolites and abundance of brachiopods suggests this facies was deposited in deeper water along the carbonate platform. Sharp-based, cm-scale beds containing brecciated mudstone and fragmented bioclastic material occur sporadically. These are interpreted as storm deposits, suggesting that although Facies 7 was deposited in deeper marine conditions, it remained above storm wave base.

Altogether, Facies 1–4 make up the Fort Vermilion Formation and are interpreted to represent the transition from a restricted lagoonal environment landward through a microbially influenced intertidal zone and into an arid, highly evaporative supratidal zone where a coastal sabkha developed along the broad, low relief eastern flank of the Peace River Arch. Subsequent flooding of the sabkha led to the deposition of evaporitic laminates interbedded with storm-driven dolomitic mudstones. Facies 5 and 6 comprise the Slave Point Formation, and each facies suggests deposition in progressively deeper water within a carbonate platform. Facies 7 represents the Waterways Formation and the introduction of terrigenous siliciclastics interbedded with allochthonous carbonates. The entirety of Facies 5–7 depicts a gradual transgression that resulted in the onlapping of Devonian strata onto the eastern flank of the Peace River Arch.

Lithium Distribution

Elevated Li was found in eight of the 41 samples, with bulk concentrations ranging from 49.4 ppm to 284.0 ppm (Fig. 4). All samples containing detectable Li were from an ~1.5-m-thick section within Facies 1, 2, and 3 of the Fort Vermilion Formation. Samples interpreted to represent a restricted lagoon (Facies 1) and those interpreted as the subtidal zone (Facies 2) had lower Li concentrations, with values ranging from 57.7 ppm to 59.1 ppm and 49.4 ppm to 109 ppm, respectively. Samples ascribed to a sabkha (Facies 3) contain the highest concentrations, with values ranging from 118 ppm to 284 ppm. The remaining 33 samples throughout Facies 4–7 in the upper Fort Vermilion, Slave Point, and Waterways Formations contained no detectable Li. Full ICP-MS results are outlined in Table 1.

The major elements aluminum (Al), iron (Fe), magnesium (Mg), potassium (K), and calcium (Ca) were measured and plotted against Li (Fig. 6). Samples with elevated Li display a strong positive correlation with Al ($R^2 = 0.964$), K ($R^2 = 0.952$), and Fe ($R^2 = 0.946$), a weak negative correlation with Ca ($R^2 = 0.623$), and no discernible trend with Mg ($R^2 = 0.291$). XRD revealed that samples with no detectable Li were composed of only anhydrite, dolomite, and quartz. In contrast, those with elevated Li were more mineralogically diverse. Facies 1 includes microcline and Mg-bearing calcite; Facies 2 includes muscovite, microcline, and Mg-bearing calcite; and Facies 3 contains muscovite, clinochlore, kaolinite, orthoclase, dickite, albite, halite, and sylvite (Fig. 4).

Petrographic analysis of the Li-rich sediments ascribed to a sabkha (Facies 3) show that they consist of anhydrite crystals, quartz grains, and aggregates of clay sized sediments hosted in a dolomitic micrite (Fig. 7). The anhydrite crystals range in size from <1.0 to 22.7 μm (mean = 12.1 μm); the quartz grains range 13.7–138.7 μm (mean = 61.3 μm); and the clay aggregates range 20.4–135.5 μm (mean = 79.9 μm). Anhydrite is ubiquitous throughout Facies 3, and most commonly occurs as subhedral to euhedral crystals. The detrital grains (quartz and clay aggregates) range from subangular to rounded and tend to be distributed regularly throughout. Although there is variation in grain size, the detrital grains are generally bimodal, with a smaller fraction of both quartz (13.7 μm to ~25.0 μm) and clay aggregates (20.4 μm to ~35.0 μm) found throughout the section. However, in some cases, higher abundances of moderate to well-sorted detrital grains are bound within loosely defined laminae. The modal percentage of quartz ranges from 5% to 15%, with the finer fraction (<40 μm) typically being monocrystalline and the coarser fraction being polycrystalline. An estimate of the modal percentage of individual minerals within the aggregate grains could not be assessed due to the clay-size fraction of the individual particles. Nonetheless, XRD identified that these grains as muscovite, clinochlore, orthoclase, kaolinite, dickite, and albite (Fig. 4). The modal percentage of clay aggregates ranges 10%–30%, with total detritals (quartz and clay aggregates) most commonly accounting for 25%–35% of the section. LA-ICP-MS analyses of each grain type shows Li concentrations in the clay aggregates range 68.7–394.4 ppm (mean = 303.7 ppm); those of the dolomitic micrite range 22.3–56.3 ppm (mean = 40.2 ppm); and the anhydrite crystals range 0.08–4.0 ppm (mean = 1.6 ppm). Given the relationship between the laser diameter (20 μm) and the size range of sediments within these rocks, we acknowledge that our results show bias toward larger grains, particularly with respect to anhydrite, where very few grains are larger than 20 μm (average ~12.1 μm). Full LA-ICP-MS results are provided in Tables 2A and 2B.

SOURCE AND SINK OF LITHIUM

Dolomite and calcite are extremely common throughout both the Fort Vermilion and Slave Point Formations, but as suggested by the weak correlations of Li with Ca ($R^2 = 0.623$) and Mg ($R^2 = 0.291$), those minerals are unlikely to be the hosts of Li. Instead, the strong correlation with Al, K, and Fe coupled with the LA-ICP-MS results demonstrate that Li is primarily hosted within micas, clay minerals, and feldspars that make up the aggregate grains. This is not unexpected given that Li^+ does not readily substitute into the crystal lattice of calcite or dolomite (Burton and Vigier, 2012), nor does it readily form carbonate phases (e.g., Li_2CO_3) except under extremely evaporitic conditions (e.g., Zheng and Liu, 1987). By contrast, the ionic radius of Li^+ is similar to Mg^{2+} and Fe^{2+} (Shannon, 1976), which means it can substitute for them in the crystal structure (Huh et al., 1998). In magmatic systems, Li characteristically behaves as an incompatible element. Although it might initially substitute for Mg^{2+} and Fe^{2+} in pyroxene and amphibole, Li typically concentrates in the increasingly felsic melt. It then substitutes in the Al^{3+} sites in micas and feldspars (Huh et al., 1998). In this regard, Maneta and Baker (2019) have shown that muscovite and alkali feldspar can incorporate up to 6700 ppm and 350 ppm Li, respectively.

During the weathering of these rocks, Li is preferentially incorporated into clay minerals compared to other soluble elements (Ronov et al., 1970). This is interpreted to be the result of

TABLE 1. INDUCTIVELY COUPLED PLASMA–MASS SPECTROMETRY DATA FOR 41 SAMPLES TAKEN FROM THE CORE

Sample ID	Li (ppm)	MgO (wt%)	CaO (wt%)	Al_2O_3 (wt%)	Fe_2O_3total (wt%)	K_2O (wt%)
#1 (1)	BDL	3.03	44.1	0.08	0.30	BDL
#1 (2)	BDL	3.12	46.9	0.09	0.33	BDL
#2 (1)	BDL	2.21	38.3	0.01	0.03	BDL
#2 (2)	BDL	1.74	26.6	0.005	0.03	BDL
#3 (1)	BDL	8.54	33.9	0.04	0.04	BDL
#3 (2)	BDL	9.17	37.8	0.05	0.04	BDL
#4 (1)	BDL	5.79	36.8	0.06	0.10	BDL
#4 (2)	BDL	5.29	33.0	0.06	0.09	BDL
#5 (1)	277 ± 2.66	11.1	23.5	1.91	1.72	0.39
#5 (2)	245 ± 2.24	9.80	21.1	1.69	1.52	0.35
#6 (1)	109 ± 1.33	7.03	25.5	0.67	0.60	0.13
#6 (2)	108 ± 0.167	7.15	26.0	0.69	0.64	0.13
#7 (1)	125 ± 0.904	5.27	29.1	0.87	0.80	0.16
#7 (2)	118 ± 1.56	5.22	27.8	0.82	0.80	0.15
#8 (1)	155 ± 0.748	9.45	23.1	0.99	0.91	0.19
#8 (2)	151 ± 1.39	9.25	22.9	0.96	0.91	0.18
#9 (1)	284 ± 0.952	8.80	17.5	2.25	1.96	0.38
#9 (2)	281 ± 2.18	8.79	17.5	2.17	2.00	0.35
#10 (1)	166 ± 1.02	13.6	20.0	0.95	0.79	0.18
#10 (2)	149 ± 1.11	14.3	20.1	0.84	0.80	0.18
#11 (1)	50.1 ± 0.552	6.68	26.6	0.27	0.29	0.06
#11 (2)	49.4 ± 0.540	6.95	26.0	0.26	0.28	0.06
#12 (1)	57.7 ± 0.511	4.43	31.6	0.49	0.53	0.12
#12 (2)	59.1 ± 0.777	4.54	32.0	0.49	0.55	0.12
#13 (1)	BDL	1.97	54.3	0.07	0.33	BDL
#13 (2)	BDL	1.99	55.1	0.06	0.33	BDL
#14 (1)	BDL	0.42	49.7	0.03	0.04	BDL
#14 (2)	BDL	0.42	49.8	0.03	0.05	BDL
#15 (1)	BDL	0.59	47.6	0.01	0.01	BDL
#15 (2)	BDL	0.65	48.4	0.01	0.01	BDL
#16 (1)	BDL	1.44	44.8	0.01	0.01	BDL
#16 (2)	BDL	1.58	46.2	0.01	0.01	BDL
#17 (1)	BDL	1.72	54.1	0.06	0.33	BDL
#17 (2)	BDL	1.74	56.4	0.07	0.34	BDL
#18 (1)	BDL	2.69	57.8	0.13	0.50	0.07
#18 (2)	BDL	2.72	57.9	0.13	0.50	0.07
#19 (1)	BDL	1.69	64.5	0.19	0.55	0.10
#19 (2)	BDL	1.77	54.8	0.19	0.50	0.09
#20 (1)	BDL	1.81	57.6	0.10	0.43	BDL
#20 (2)	BDL	1.82	58.8	0.11	0.45	BDL
#21 (1)	BDL	0.69	61.0	0.01	0.10	BDL
#21 (2)	BDL	0.72	63.5	0.01	0.10	BDL
#22 (1)	BDL	0.63	58.1	0.13	0.46	0.06
#22 (2)	BDL	0.63	57.2	0.12	0.47	0.07
#23 (1)	BDL	0.59	63.2	0.00	0.05	BDL
#23 (2)	BDL	0.62	63.4	0.00	0.05	BDL
#24 (1)	BDL	0.81	63.2	0.02	0.36	BDL
#24 (2)	BDL	0.81	66.6	0.02	0.35	BDL
#25 (1)	BDL	0.83	63.5	0.04	0.37	BDL
#25 (2)	BDL	0.86	62.8	0.03	0.35	BDL
#26 (1)	BDL	0.76	63.1	0.03	0.38	BDL
#26 (2)	BDL	0.76	64.6	0.03	0.38	BDL
#27 (1)	BDL	3.78	50.5	0.43	1.32	0.20
#27 (2)	BDL	3.80	49.5	0.44	1.30	0.20
#28 (1)	BDL	4.68	47.4	0.55	1.67	0.23
#28 (2)	BDL	4.49	50.0	0.57	1.62	0.23
#29 (1)	BDL	3.12	54.0	0.39	1.11	0.17
#29 (2)	BDL	3.15	53.9	0.42	1.13	0.18
#30 (1)	BDL	2.55	58.3	0.36	0.88	0.16
#30 (2)	BDL	2.49	55.5	0.38	0.84	0.15
#31 (1)	BDL	1.81	62.0	0.23	0.69	0.12
#31 (2)	BDL	1.99	62.3	0.24	0.60	0.11
#32 (1)	BDL	2.60	55.3	0.40	1.06	0.17
#32 (2)	BDL	2.72	56.2	0.40	1.07	0.18
#33 (1)	BDL	1.24	69.7	0.13	0.36	0.07
#33 (2)	BDL	1.22	65.8	0.15	0.35	0.07
#34 (1)	BDL	1.04	66.9	0.07	0.37	BDL
#34 (2)	BDL	1.03	66.5	0.08	0.35	BDL
#35 (1)	BDL	1.07	61.0	0.10	0.42	BDL
#35 (2)	BDL	1.05	67.2	0.10	0.45	BDL
#36 (1)	BDL	1.66	59.7	0.31	0.96	0.14
#36 (2)	BDL	1.67	61.8	0.32	1.05	0.15
#37 (1)	BDL	0.76	68.1	0.02	0.17	BDL
#37 (2)	BDL	0.71	67.3	0.02	0.17	BDL
#38 (1)	BDL	0.67	70.7	0.03	0.21	BDL
#38 (2)	BDL	0.65	66.7	0.03	0.22	BDL
#39 (1)	BDL	0.96	55.8	0.45	1.46	0.14
#39 (2)	BDL	0.93	56.1	0.40	1.49	0.15
#40 (1)	BDL	1.49	56.7	0.20	0.78	0.09
#40 (2)	BDL	1.51	57.5	0.21	0.79	0.10
#41 (1)	BDL	0.78	68.0	0.03	0.10	BDL
#41 (2)	BDL	0.79	74.7	0.03	0.10	BDL

Notes: All samples were analyzed in duplicate. Li is reported in parts per million (ppm) and major elements are reported in weight percent oxide (wt%). Detectable lithium was found in samples #5 through #12. Samples listed as "BDL" were below the detection limit of the instrument (detection limit: Li = 0.25 ppm; K = 450 ppm).

isomorphic substitution of Al^{3+} by Mg^{2+} in the octahedral layer of a clay, leaving a vacant space for Li^+ to fill and neutralize the overall charge (Heier and Billings, 1978). Particularly in laterites, Ronov et al. (1970) has shown increased Li content with the presence of kaolinite and a sharp drop in Li content when kaolinite has completely weathered to goethite and aluminum hydroxides. Those authors suggest this reflects a direct link between Li content, kaolinite, and the extent of weathering in soils.

Lazowski et al. (2025) examined the Precambrian basement of the PRA and five of its overlying siliciclastic and carbonate units for their Li concentration and isotopic values. They examined core both within and outside of the major fault zone suggested to be responsible for the post-depositional influx of Li-rich hydrothermal fluids and found no visual, mineralogical, or geochemical evidence of hydrothermal alteration in any of the five units. Instead, they observed that Li concentrations and δ^7Li values vary by 167 ppm and 22.0‰, respectively, and that these distributions are facies-dependent, displaying a typical weathering profile across all core regardless of their locations (Lazowski et al., 2025). Burwash (1957) and Burwash and Krupicka (1969, 1970) examined basement rocks of the Western Canada Sedimentary Basin and identified a zone of K-metasomatism trending northeast through the PRA and into a large portion of west-central Alberta. They found that metasomatic recrystallization significantly increased the relative proportion of silicate and alteration minerals in these rocks and suggested the decrease in average density of this K-metasomatized zone was responsible for upward movement of the PRA (Burwash and Krupicka, 1970). Notably, the altered rocks showed the largest changes in potassium feldspar, muscovite, and epidote content, increasing 73%, 383%, and 484%, respectively (Burwash and Krupicka, 1970). In their study examining Li concentrations and δ^7Li values of the PRA, Lazowski et al. (2025) found that recrystallized basement (103.4–109.8 ppm) hosts, on average, 4× more Li than unaltered basement (21.7–29.0 ppm) and 5× the Li of bulk continental crust (Teng et al., 2004; Tomascak et al., 2016). They suggest that K-metasomatism played a key role in Li enrichment of the PRA basement and that muscovite and siderophyllite are the major host phases within these crystalline rocks. Sedimentological and mineralogical analysis of the overlying siliciclastics and carbonates found that these sediments were derived from the PRA and transported basinward along a system of laterally migrating fluvial channels into deltaic and shallow marine environments of the surrounding basin (Lazowski et al., 2025). Most notably, paleosols that formed along the banks

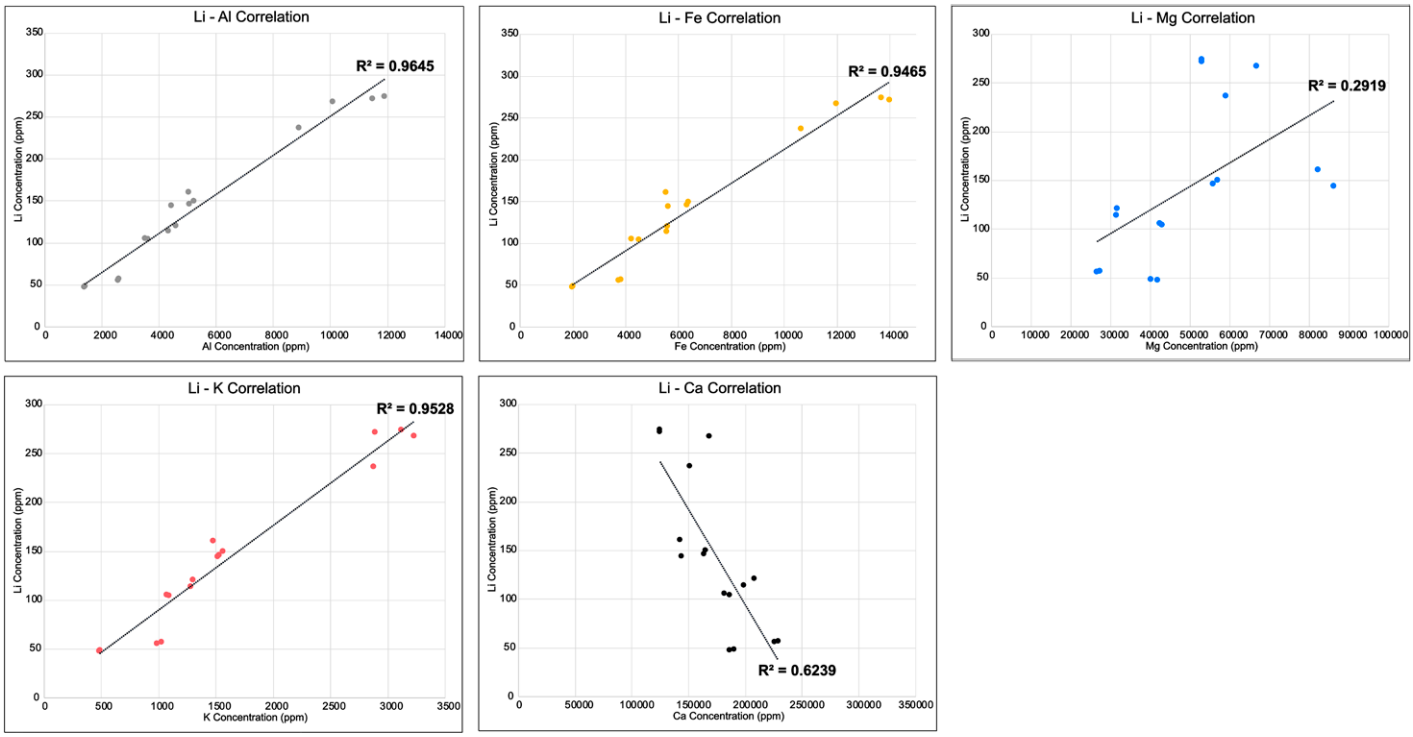

Figure 6. Correlation charts of bulk lithium with other major elements measured in the samples. Lithium shows exceptionally high R^2 values with Al (0.964), K (0.952), and Fe (0.946), and a weak negative correlation exists with Ca (0.623). No discernable trend is observed with Mg.

of the fluvial system draining the PRA displayed bulk Li concentrations up to ~167 ppm, and X-ray diffraction revealed that these sediments are composed of a nearly identical mineralogy to the Li-rich clay aggregates identified in this study (quartz, microcline, orthoclase, muscovite, and kaolinite).

Given the propensity for Li to be associated with primary felsic minerals and secondary clay minerals, along with the mineralogical, geochemical, and sedimentological similarities between the Li-rich clay aggregates in this study and the paleosols examined by Lazowski et al. (2025), it is most likely that the Li-rich clay aggregates in Facies 1–3 of the Fort Vermilion Formation originate from the weathering of Precambrian basement rock of the PRA. We propose that micas and feldspars containing trace Li were directly weathered from those exposed felsic rocks and accumulated in the overlying regolith. As the regolith underwent further chemical weathering, some of the primary igneous minerals were altered into secondary clays, and the Li that was mobilized during this process became either selectively fixed into the clays' crystal structure or adsorbed onto these sediments (Stoffynegli and Mackenzie, 1984). These sediments were simultaneously transported basinward along a fluvial-deltaic system where extensive Li-bearing paleosols formed along the banks of these channels (Lazowski et al., 2025). The resulting paleosols contained a mixture of clay sized, Li-bearing primary igneous minerals and secondary clays.

From the PRA, these Li-rich sediments could have been transported into the surrounding marginal-marine environments through two mechanisms: (1) drainage into the basin followed by alongshore migration of the fine detrital grains or (2) aeolian transport. In the case of drainage, fluvial transport, combined with subsequent reworking and winnowing by tides and longshore currents, leads to sediment sorting and the accumulation of sands in foreshore beaches, and nearshore sand bars, spits, and barrier islands (Nair et al., 1982; Pemberton et al., 2012; Nabhan and Yang, 2018). These traits are observed in modern, evaporative coastal environments such as Al Qahmah, Saudi Arabia, where poorly sorted fluvial and deltaic sediments delivered to the coast are winnowed, reworked, and redistributed by longshore currents, forming extensive beaches composed of well-sorted sands (Nabhan and Yang, 2018). In these environments, foreshore deposits characteristically comprise well-sorted, fine sands displaying planar laminae with distinct swash zone laminae, whereas nearshore bars are composed of fine- to medium-grained sands exhibiting planar to trough cross-stratification (Pemberton et al., 2012; Nabhan and Yang, 2018). The mud and clay-sized sediments winnowed from the detritals during wave and alongshore reworking accumulate in the subtidal zone, forming the source material for tidal flat accretion. However, transport from the shallow, low-energy lagoons into intertidal and supratidal zones is generally limited to storm-tide conditions, during which muds are stirred into suspension and pushed landward onto the flats (Shinn, 1983). These events result in distinct and episodic, cm-scale beds of clay-sized sediments within intertidal and supratidal deposits.

With respect to aeolian transport, modern sabkha deposits from Al Qahmah, Saudi Arabia, are characterized by a bimodal distribution of regularly dispersed silt- to coarse sand-sized siliciclastics that are continentally derived from nearby igneous rocks (Fryberger et al., 1983; Nabhan and Yang, 2018). Their bimodal grain size distribution is interpreted to reflect sediment mixing from fluctuating wind conditions and variable source terrains (Nabhan and Yang, 2018). Moreover, wind-borne sediments tend to be mineralogically representative of their source material, with silt-sized quartz, along with mud-sized micas and clays, being ubiquitous in aeolian sediments (Pye, 1987).

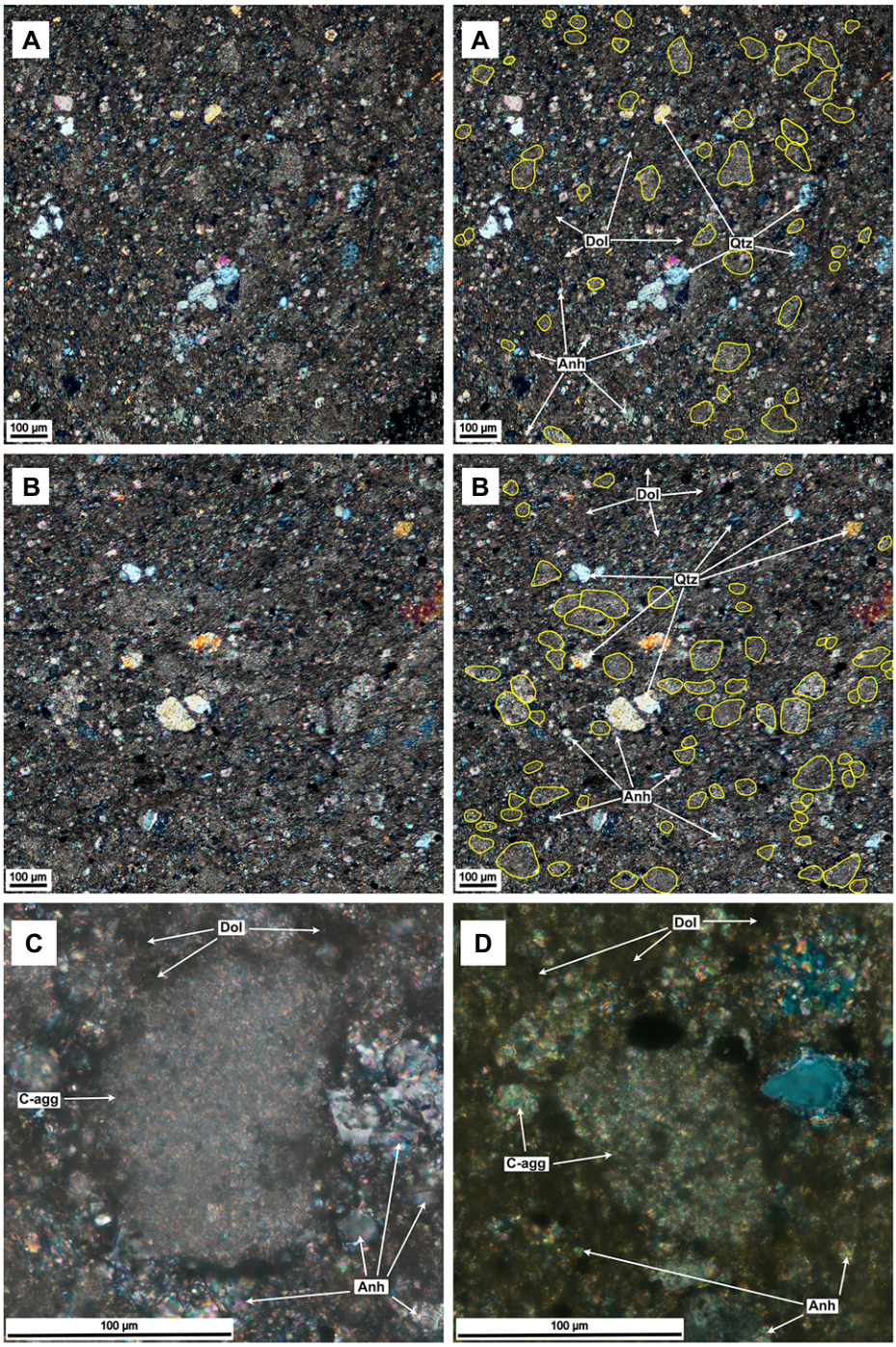

Figure 7. Representative thin sections (cross polarized) of the sabkha facies showing subangular quartz grains, anhydrite crystals, and subrounded aggregates of clay sized particles hosted in a dolomitic micrite. (A) Poorly sorted and regularly distributed sediments throughout evaporites and carbonates. (B) Moderately sorted sediments within poorly define laminae. (C, D) Clay aggregates hosted in anhydrite and dolomitic micrite. (Bottom) Laser ablation–inductively coupled plasma–mass spectrometry data and the size range of each grain type. Clay aggregates are outlined in yellow. Dol—dolomite; Qtz—quartz; Anh—anhydrite; C-agg—clay aggregate.

Grain type	Size range (mean) (µm)	Li Concentration range (mean) (ppm)
Clay aggregates	20.4 - 135.5 (79.9)	68.7 - 394 (304)
Dolomitic micrite	N/A	22.3 - 56.3 (40.2)
Anhydrite	<1.0 - 22.7 (12.1)	0.08 - 4.0 (1.6)
Quartz	13.7 - 138.7 (61.3)	N/A

Although previous work by Lazowski et al. (2025) demonstrated the fluvial-deltaic transport and deposition of siliciclastics derived from the PRA, their study describes fluvial deposits as very fine–pebbly sandstones, characterized by sharp-based packages of low angle to tabular cross-bedding. Basinward, deltaic sediments become finer-grained and exhibit current ripples, flaser and wavy bedding, and periodic bioturbation (Lazowski et al., 2025). Notably, they also observed that increased mineralogical and textural maturity, resulting from hydraulic reworking in the marginal marine environments, correlates with a decline in Li concentrations within these sediments (Lazowski et al., 2025).

The detrital grains identified in this study lack all sedimentological and geochemical traits of fluvial transport or marine reworking. Instead, they display many of the same characteristics associated with modern sabkhas. These aggregate grains are texturally bimodal, ranging from silt to fine sand, and they are mineralogically distinct from previously identified fluvial sediments. Instead, they exhibit a nearly perfect match with the texture, mineralogy, and high Li concentrations of paleosols identified on the PRA (Lazowski et al., 2025). Where present, these aggregate grains are evenly distributed throughout these deposits. Despite the well-developed planar laminae and occasional storm beds common in these evaporitic settings, the detrital grains themselves are not confined to individual laminae or lamina-sets. This indicates that their deposition was independent of the prevailing hydraulic conditions (Fig. 7). However, in some instances, moderately to well-sorted grains appear loosely bound within weakly defined laminae. We interpret these features as evidence of episodic sabkha water fluctuations, during which wind-transported sediments flocculated within the brine and were subsequently cemented by the precipitation of evaporite minerals after the water table receded (Fryberger et al., 1983; Warren, 2016). Given the textural, mineralogical, and geochemical characteristics of these detritals, coupled with their widespread distribution, it is unlikely that they were deposited via drainage and alongshore transport. Instead, we interpret them as wind-derived sediments, consistent with previous studies (i.e., Fryberger et al., 1983; Nabhan and Yang, 2018). We propose that the Li-rich silt- to fine-sand–sized

TABLE 2A. (TOP) LASER ABLATION–INDUCTIVELY COUPLED PLASMA–MASS SPECTROMETRY DATA OF 36 SPOT ANALYSES TAKEN FROM SAMPLES #5 AND #9

Grain type	Li (ppm)	Mg (ppm)	Al (ppm)	Si (ppm)	K (ppm)	Ca (ppm)	Fe (ppm)
Clay aggregate	258	54,900	15,700	49,800	5030	196,000	3130
Clay aggregate	265	65,700	17,300	57,500	7120	166,000	3580
Clay aggregate	207	20,100	15,200	38,900	3430	260,000	3460
Clay aggregate	319	44,900	25,600	96,300	11,200	95,900	4270
Clay aggregate	262	53,500	15,800	74,000	8980	151,000	4010
Clay aggregate	157	56,000	14,200	21,600	23,200	249,000	3830
Clay aggregate	371	41,100	35,000	90,000	6830	90,100	5110
Clay aggregate	293	48,300	23,000	65,000	5670	149,000	4310
Clay aggregate	246	51,400	28,000	75,100	5030	132,000	4770
Clay aggregate	308	25,900	30,800	83,200	8070	152,000	5850
Clay aggregate	371	46,500	30,800	80,100	6490	125,000	19,400
Clay aggregate	352	82,500	23,200	61,700	9660	235,000	5970
Clay aggregate	332	43,600	10,300	32,700	3110	389,000	3680
Clay aggregate	315	52,600	19,100	61,300	8400	184,000	5120
Clay aggregate	357	35,300	38,600	95,600	28,200	85,700	31,600
Clay aggregate	383	31,600	20,400	59,100	13,900	214,000	5690
Clay aggregate	314	49,500	18,100	77,100	5990	169,000	4850
Clay aggregate	394	29,900	18,900	47,600	6020	276,000	3700
Clay aggregate	351	41,900	20,500	75,900	7060	161,000	19,100
Clay aggregate	364	30,500	20,100	50,700	11,100	249,000	4730
Clay aggregate	68.7	59,800	27,700	42,500	6830	164,000	4410
Clay aggregate	388	78,000	13,000	42,800	3990	189,000	2920
Clay aggregate	298	56,100	15,800	69,500	5970	114,000	5180
Clay aggregate	323	71,300	12,100	47,500	3570	156,000	3850
Clay aggregate	260	68,600	14,500	48,600	3850	160,000	2860
Clay aggregate	263	77,900	9210	42,800	4150	176,000	2780
Clay aggregate	378	70,800	11,000	47,200	5560	138,000	3250
Anhydrite	0.084	12.5	BDL	BDL	BDL	435,000	634
Anhydrite	0.183	14.3	0.882	1530	BDL	340,000	699
Anhydrite	4.03	1110	270	BDL	63.7	343,000	756
Anhydrite	2.13	81.3	147	BDL	22.1	326,000	692
Dolomitic micrite	22.3	25,500	2110	365	3520	346,000	1790
Dolomitic micrite	44.3	43,800	2930	8190	6460	307,000	1720
Dolomitic micrite	45.4	36,300	3180	1160	7020	331,000	2070
Dolomitic micrite	32.7	59,500	10,700	32,400	863	350,000	1370
Dolomitic micrite	56.3	94,000	994	647	357	259,000	1490

Notes: Li concentrations within the clay aggregates, anhydrite, and micrite range 68.7–394 ppm, 223.–56.3 ppm, and 0.08–4.0 ppm, respectively. All elements measured within 0.2% of accepted U.S. National Institute of Standards and Technology Standard Reference Materials 610 values.

aggregates found in the Fort Vermilion Formation originated from paleosols on the high-relief PRA and were transported by wind into the surrounding marginal-marine settings (Fig. 8).

At the facies level, variations in the proportion of detritals and resulting bulk Li concentrations are closely linked to environmental factors. The sabkha facies show the highest Li concentrations, primarily due to a lack of reworking by hydraulic processes, thereby allowing for the accumulation and preservation of aeolian sediments. In contrast, facies within the intertidal and subtidal zones display lower Li concentrations, likely due to sediment reworking and Li desorption in seawater. The lower Li concentrations observed in intertidal units resulted from more hydraulically energetic conditions. During low tide, aeolian sediments accumulated on the flats, but at high tide, increased water movement led to partial removal of Li prior to burial. Similar observations have been made in the Persian Gulf, where algal mats and carbonate muds of the intertidal zone act as a sticky trap, capturing windblown sediments from the Zagros Mountains of Iran during low tide and redistributing them upon tidal influx (Shinn, 1983). Within the subtidal zone, tidal and wave action would have diluted Li-rich aggregates across the shallow, restricted lagoon, dispersing some sediments before they could settle.

Experimental results from Taylor et al. (2019) support our hypothesis that micas, clay minerals, and feldspars—in the form of aggregate particles—were the main transport vector for Li into the dolomitic micrite. Their findings demonstrate that dolomite formed at burial temperatures can incorporate Li, provided a local source is available. We propose that at least some of the dolomite was initially deposited as high-Mg aragonite, and that following deposition, Li that was initially adsorbed onto clay aggregates ultimately diffused into the proximal dolomitic matrix during burial and dolomitization. In this regard, we interpret the generally low Li concentrations of the dolomitic micrite (mean = 40.2 ppm)—in comparison with the clay aggregates (mean = 303.7 ppm)—to suggest that the majority of the Li remained fixed within the phyllosilicates, with only a fraction being mobilized and incorporated into the dolomitic matrix. This interpretation supports the hypothesis that Li was desorbed from kaolinite after deposition, at least partially, within the evaporitic setting (Hoyer et al., 2015).

TABLE 2B. REFERENCE MATERIAL NIST610 MEASUREMENTS

Element	Measured value	NIST610 accepted value	% diff	Variation (%RSD)	Minimum measurement	Maximum measurement
Li	468.9	468	0.20	5.29	448	505
Mg	432.0	432	0.01	4.11	413	448
Al	10,801	10,797	0.04	2.89	10,539	11,056
Si	326,948	327,180	−0.07	5.71	309,752	343,168
K	463.7	464	−0.06	4.82	443	483
Ca	82,206	82,144	0.07	3.5	79,494	84,736
Fe	457.7	458	−0.06	4.13	435	475
Th	457.2	457.2	0.00	2.73	440	465
U	462.1	461.5	0.12	4.74	445	486

Notes: "Measured value" represents the mean across all bracketing standard measurements. All elements measured within 0.2% of accepted U.S. National Institute of Standards and Technology Standard Reference Materials (NIST) 610 values. RSD—relative standard deviation.

Quartz grains identified in this study tend to be subangular to subrounded, with an average grain size of 61.3 μm. In contrast, aggregate grains that range from subangular to rounded and that have a slightly larger average size of 79.9 μm are present, although a smaller fraction of both quartz (13.7 μm to ~25.0 μm) and aggregate grains (20.4 μm to ~35.0 μm) exists throughout the section. Tsoar and Pye (1987) reported that quartz particles as large as 70 μm can be suspended and transported on the order of kilome-

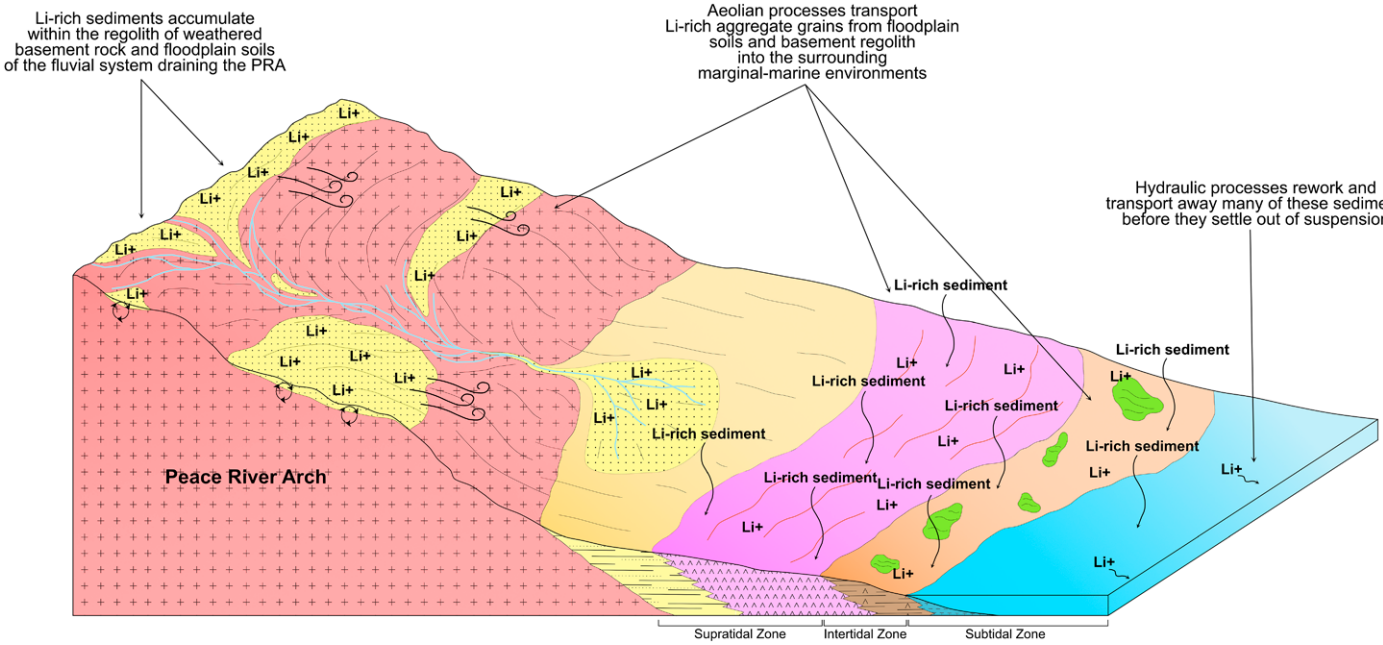

Figure 8. Depositional model of Li within the Fort Vermilion Formation. Paleosols weathered from the Peace River Arch host lithium in feldspars, micas, and clays. These sediments were windblown from the high-relief topography of the nearby arch and deposited across the surrounding marginal-marine environments. The most restricted, supratidal zone was able to trap windblown sediments most efficiently, whereas wave and tidal action of the intertidal and subtidal zones transported away some of these aeolian sediments before they could be buried.

ters, and observations from wind-eroded soils of Texas, New Mexico, Colorado, and Oklahoma, USA, found suspended particles up to 80 μm (Gillette et al., 1978). A bimodal or polymodal grain size distribution is commonly reported in aeolian sediments and are ascribed to two processes: (1) wind-blown sediments transporting a mixture of local and regional components, and (2) clay-sized particles are mainly transported as silt-size aggregates, and coatings on larger grains, both of which may become disaggregated during deposition or through grain-on-grain collisions while in suspension (Pye, 1987; Smalley and Vita Finzi, 1968). Particle size analysis from the Harmattan dust in Mali, West Africa, shows a polymodal distribution, with three size groups ranging from <5 μm, to 20–40 μm, to 50–70 μm that are respectively interpreted to indicate aeolian mixing from far-traveled, regional, and local sediment sources (McTainsh et al., 1997). A more detailed assessment of Harmattan dust in northern Nigeria identified quartz, feldspars, and clay aggregates that were locally sourced and associated with soil-forming processes (Whalley and Smith, 1981). Like modern aeolian systems, we interpret the minor variations in grain size and sorting to be the result of shifting local wind patterns (i.e., wind velocity) and sediment mixing from multiple sources (Sinclair, 1988; McTainsh et al., 1997; Nabhan and Yang, 2018). Lazowski et al. (2025) show that although paleosols from the PRA are generally composed of very mature, clay- to silt-sized grains, a range of paleosol maturities exist with distance from the crystalline source rock.

An aeolian transport mechanism further suggests that Li should be widespread throughout the Fort Vermilion Formation, although influenced by wind-transport direction. Earlier work by Jansa and Fischbuch (1974) reported a complete lack of terrigenous quartz grains in both lagoon and intertidal facies of the Fort Vermilion Formation, suggesting a predominantly onshore wind direction during deposition (Fig. 9). In the Middle Devonian, the PRA resided south of the palaeoequator, where southeasterlies dominated regional wind patterns (Witzke and Heckel, 1988), offering the possibility that Li-rich sediments were also transported from exposed craton to the east (Fig. 9). Long-term suspension can transport particles on the order of thousands of kilometers; however, these particles have a known upper size limit of ~20 μm (Nickling and Neuman, 2009). Given the smaller fraction of our quartz and aggregate grains, we cannot discount that some of these sediments may, in part, originate from the exposed Canadian Shield (to the northeast), although a detailed investigation into the Li potential of these strata is still lacking. The study area of Jansa and Fischbuch (1974) is ~150–200 km south of the core location used for this study, in a region where Middle Devonian southeasterlies traveled in a predominantly onshore direction and would have needed to transport airborne sediments on the order of hundreds to thousands of kilometers from exposed craton to the east, making it unlikely that detrital grains of this size fraction (>20 μm) would have reached their study area. Our results differ in that this core is positioned east-northeast of the PRA, in an area where regional southeasterlies likely deflected around the high-relief cratonic uplift, funneling local wind patterns roughly parallel to the trend of the PRA. The Fort Vermillion Formation is interpreted to have been deposited during low sea level or a period of slight regression, prior to the overall transgressive phase of the Middle Devonian (Jansa and Fischbuch, 1974; Keith, 1990). This region was likely on the order of kilometers to tens of kilometers away from the PRA and well within the known limits of aeolian suspension transport (Tsoar and Pye, 1987).

In a global context, the generation and transport of wind-borne sediments are widely recognized as an important process influencing Earth's surface systems (Kohfeld and Harrison., 2001; McGee et al., 2016). Aeolian transport is responsible for redistributing between 1.0 and 3.0 gigatons of sediment annually, facilitating the global dispersal of vast quantities of trace metals (Cakmur et al., 2006; Tanaka and Chiba, 2006). While modern rivers account for an estimated 50% of Li input into the oceans, their concentrations

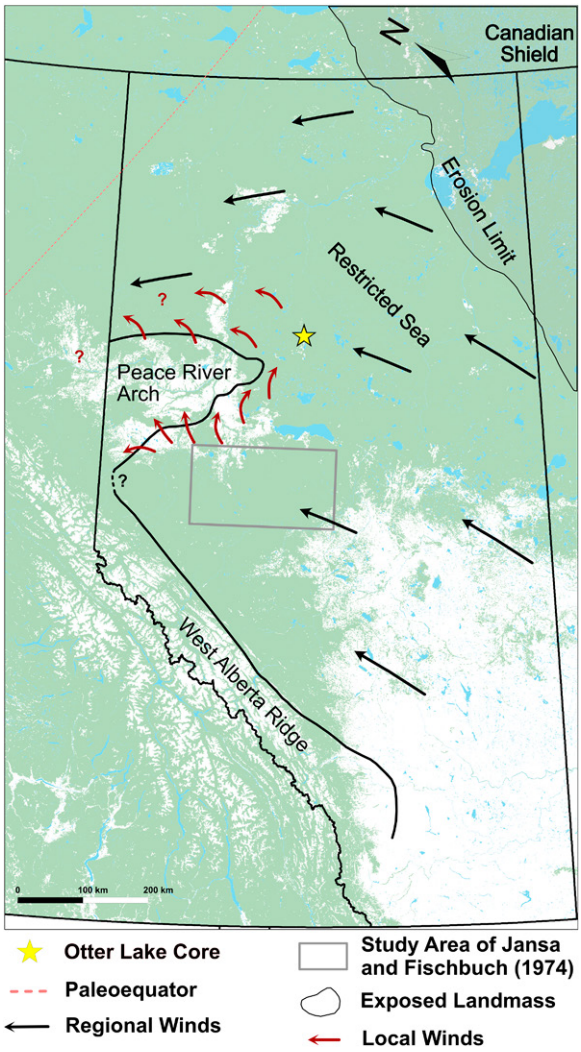

Figure 9. Hypothetical regional and local wind patterns around the Peace River Arch (PRA). In the Middle Devonian, the PRA was situated south of the palaeoequator (pink dashed line) in a region where southeasterlies would have been the predominant wind direction. Previous work by Jansa and Fischbuch (1974) reported a lack of terrigenous quartz grains and suggested a predominantly onshore wind direction during deposition of the Fort Vermilion in their study area (gray box). We suggest local winds deflected northnortheast around the high-relief PRA, in a predominantly offshore direction, and transported regolith weathered from the exposed basement into the surrounding marginal-marine setting. Outlines of exposed landmass during the Upper Devonian (Frasnian) are modified from Campbell (1992). Erosional limit modified from Oldale and Munday (1994).

(~1.8 ppb) are significantly lower compared to terrestrial clay minerals (~5.0–300 ppm), suggesting that a substantial portion of Li derived from primary rocks remains stored within secondary clays on the continents (Huh et al., 1998; Tomascak et al., 2016; Pogge von Strandmann et al., 2020). Although aeolian sediments are often texturally and mineralogically mature, our findings suggest that wind-driven redistribution of sediments derived from crystalline rocks plays a greater role in the accumulation of Li than previously recognized. Furthermore, the paleogeographic distribution patterns of these sediments may be predictable, offering new insights into potential alternative Li resources.

CONCLUSION

To test the hypothesis of Li-enriched evaporites within the Western Canada Sedimentary Basin, we examine Devonian-aged carbonates and evaporites from an interval known for hosting high Li-brine concentrations. Our findings challenge previous assumptions that Li is primarily hosted within late-stage evaporitic minerals, revealing instead that it resides within silt- to very fine sand–sized aggregate grains composed of clay-sized primary igneous minerals and secondary clays. Lithofacies and geochemical analysis revealed that these sediments were sourced from nearby Li-rich regolith and paleosols that developed along uplifted crystalline basement of the PRA and were subsequently transported by wind into the surrounding marine evaporitic basin. Our results demonstrate that the deposition and preservation of aeolian sediments are facies dependent, with lower-energy environments (i.e., supratidal zone) acting as efficient traps for windblown sediments. By contrast, higher-energy environments, such as the subtidal and intertidal zones, experience wave and tidal reworking that either transports these sediments away or dilutes them prior to settling and burial.

This study is the first to detail the role of aeolian transport in Li accumulation within sedimentary basins. With individual grains hosting up to 394 ppm Li and given the well-established association between Li deposits and felsic igneous systems, our results suggest that, in addition to previously described fluvial transport and evaporation concentration mechanisms, aeolian processes may supplement the emplacement of Li across a sedimentary basin and play a more significant role than previously recognized. Our findings underscore the critical link between Li-brine distributions and syndepositional processes in ancient sedimentary basins, highlighting the need to establish a robust geological framework to inform global Li exploration efforts. This predictive approach can be applied to sedimentary basins worldwide, offering new insights into Li resource development.

ACKNOWLEDGMENTS

Funding for this research was generously provided by the Natural Sciences and Engineering Research Council of Canada (NSERC) Discovery Grants to Murray Gingras (RGPIN-2020-0513) and Kurt Konhauser (RGPIN-2020-05189). We extend our sincere thanks to Troy Rasbury, Rajat Mazumder, and two anonymous reviewers for their valuable and constructive feedback. We also express gratitude to Andrew Locock for his insightful discussions that helped shape the outcomes of this research.

REFERENCES CITED

Agusdinata, D.B., Liu, W., Eakin, H., and Romero, H., 2018, Socio-environmental impacts of lithium mineral extraction: Towards a research agenda: Environmental Research Letters, v. 13, no. 12, p. 123001, https://doi.org/10.1088/1748-9326/aae9b1.

Aitken, J.D., 1971, Control of lower Paleozoic sedimentary facies by the Kicking Horse Rim, Southern Rocky Mountains, Canada: Bulletin of Canadian Petroleum Geology, v. 19, p. 557–569, https://doi.org/10.35767/gscpgbull.19.3.557.

Ambrose, H., and Kendall, A., 2019, Understanding the future of lithium: Part 1, resource model: Journal of Industrial Ecology, v. 24, p. 80–89, https://doi.org/10.1111/jiec.12949.

Balshaw, K.E., 2010, Sedimentology and Stratigraphy of the Granite Wash: Contact Rapids and Keg River Sandstone (Red Earth Area) [Master's Thesis]: Edmonton, Alberta, Canada, University of Alberta, 266 p., https://doi.org/10.7939/R3H12VG45.

Beaumont, C., Quinlan, G.M., and Stockmal, G.S., 1993, The evolution of the Western Interior Basin: Causes, consequences and unsolved problems, *in* Caldwell, W.G.E., and Kauffman, E.G., eds., Evolution of the Western Interior Basin: Geological Association of Canada Special Paper 39, p. 97–117.

Benson, T.R., Coble, M.A., Rytuba, J.J., and Mahood, G.A., 2017, Lithium enrichment in intracontinental rhyolite magmas leads to Li deposits in caldera basins: Nature Communications, v. 8, 270, https://doi.org/10.1038/s41467-017-00234-y.

Bond, G.C., and Kominz, M.A., 1984, Construction of tectonic subsidence curves for the early Paleozoic miogeocline, southern Canadian Rocky Mountains: Implications for subsidence mechanisms, age of breakup and crustal thinning: Geological Society of America Bulletin, v. 95, p. 155–173, https://doi.org/10.1130/0016-7606(1984)95<155:COTSCF>2.0.CO;2.

Bowell, R.J., Lagos, L., de los Hoyos, C.R., and Declercq, J., 2020, Classification and characteristics of natural lith-

ium resources: Elements. v. 16, p. 259–264, https://doi.org/10.2138/gselements.16.4.259.

Bradley, D.C., Munk, L., Jochens, H., Hynek, S., and Labay, K., 2013, A preliminary deposit model for lithium brines: U.S. Geological Survey Open File Report 2013-1006, 6 p., https://doi.org/10.3133/ofr20131006.

Burwash, R.A., 1957, Reconnaissance of subsurface Precambrian of Alberta: The American Association of Petroleum Geologists Bulletin, v. 41, p. 70–103, https://doi.org/10.1306/5CEAE601-16BB-11D7-8645000102C1865D.

Burwash, R.A., and Krupicka, J., 1969, Cratonic reactivation in the Precambrian basement of western Canada. I. Deformation and chemistry: Canadian Journal of Earth Sciences, v. 6, https://doi.org/10.1139/e69-140.

Burwash, R.A., and Krupicka, J., 1970, Cratonic reactivation in the Precambrian basement of western Canada. Part II: Canadian Journal of Earth Sciences, v. 7, https://doi.org/10.1139/e70-120.

Burton, K.W., and Vigier, N., 2012, Lithium isotopes as tracers in marine and terrestrial environments, *in* Baskaran, M., ed., Handbook of Environmental Isotope Geochemistry: Berlin, Heidelberg, Springer, Advances in Isotope Geochemistry, p. 41–59, https://doi.org/10.1007/978-3-642-10637-8_4.

Buyung Agusdinata, D., Liu, W., Eakin, H., and Romero, H., 2018, Socio-environmental impacts of lithium mineral extraction: Towards a research agenda: Environmental Research Letters, v. 13, 123001, https://doi.org/10.1088/1748-9326/aae9b1.

Cakmur, R.V., Miller, R.L., Perlwitz, J., Geogdzhayev, I.V., Ginoux, P., Koch, D., and Zender, C.S., 2006, Constraining the magnitude of the global dust cycle by minimizing the difference between a model and observations: Journal of Geophysical Research: Atmospheres, v. 111, https://doi.org/10.1029/2005JD005791.

Campbell, C.V., 1992, Beaverhill Lake megasequence *in* Wendte, J.C., Stoakes, F.A., and Campbell, C.V., eds., Devonian-Early Mississippian Carbonates of the Western Canada Sedimentary Basin: A Sequence Stratigraphic Framework: Society for Sedimentary Geology (SEPM) Short Course Notes, v. 28, p. 163–181, https://doi.org/10.2110/scn.92.28.

Cant, D.J., 1988, Regional structure and development of the Peace River Arch, Alberta: A Paleozoic failed-rift system?: Bulletin of Canadian Petroleum Geology, v. 36, p. 284–295, https://doi.org/10.35767/gscpgbull.36.3.284.

Castor, S.B., and Henry, C.D., 2020, Lithium-rich claystone in the McDermitt caldera, Nevada, USA: Geologic, Mineralogical, and Geochemical Characteristics and Possible Origin: Minerals (Basel), v. 10, 68, https://doi.org/10.3390/min10010068.

Černý, P., and Ercit, T.S., 2005, The classification of granitic pegmatites revisited: The Canadian Mineralogist, v. 43, p. 2005–2026, https://doi.org/10.2113/gscanmin.43.6.2005.

Coffey, D.M., Munk, L.A., Ibarra, D.E., Butler, K.L., Boutt, D.F., and Jenckes, J., 2021, Lithium storage and release from lacustrine sediments: Implications for lithium enrichment and sustainability in continental brines: Geochemistry, Geophysics, Geosystems, v. 22, https://doi.org/10.1029/2021GC009916.

Collins, A.G., 1976, Lithium abundances in oilfield waters, *in* Vine, J.D., ed., Lithium Resources and Requirements by the Year 2000: U.S. Geological Survey Professional Paper 1005, p. 116–123, https://doi.org/10.3133/pp1005.

Connolly, C.A., Walter, L.M., Baadsgaard, H., and Longstaffe, F.J., 1990a, Origin and evolution of formation waters, Alberta Basin, Western Canada Sedimentary Basin. I. Chemistry: Applied Geochemistry, v. 5, p. 375–395, https://doi.org/10.1016/0883-2927(90)90016-X.

Connolly, C.A., Walter, L.M., Baadsgaard, H., and Longstaffe, F.J., 1990b, Origin and evolution of formation waters, Alberta Basin, Western Canada Sedimentary Basin. II. Isotope systematics and water mixing: Applied Geochemistry, v. 5, p. 397–413, https://doi.org/10.1016/0883-2927(90)90017-Y.

Dec, T., Hein, J.H., and Trotter, R.J., 1996, Granite Wash alluvial fans, fan-deltas and tidal environments, northwestern Alberta: Implications for controls on distribution of Devonian clastic wedges associated with the Peace River Arch: Bulletin of Canadian Petroleum Geology, v. 44, p. 541–565, https://doi.org/10.35767/gscpgbull.44.3.541.

Deveaud, S., Millot, R., and Villaros, A., 2015, The genesis of LCT-type granitic pegmatites, as illustrated by lithium isotopes in micas: Chemical Geology, v. 411, p. 97–111, https://doi.org/10.1016/j.chemgeo.2015.06.029.

Dugamin, E.J.M., Richard, A., Cathelineau, M., Boiron, M.-C., Despinois, F., and Brisset, A., 2021, Groundwater in sedimentary basins as potential lithium resource: A global prospective study: Scientific Reports, v. 11, 21091, https://doi.org/10.1038/s41598-021-99912-7.

Eccles, D.R., and Berhane, H., 2011, Geological introduction to lithium-rich formation water with emphasis on the Fox Creek area of west-central Alberta (NTS 83F and 83 K): Energy Resources Conservation Board, ERCB/AGS Open File Report 2011-10, 22 p., https://ags.aer.ca/publications/all-publications/ofr-2011-10 (accessed April 2025).

Evans, K., 2014, Lithium, *in* Gunn, G., ed., Critical Metals Handbook: John Wiley & Sons, p. 230–260, https://doi.org/10.1002/9781118755341.ch10.

Flexer, V., Baspineiro, C.F., and Galli, C.I., 2018, Lithium recovery from brines: A vital raw material for green energies with a potential environmental impact in its mining and processing: The Science of the Total Environment, v. 639, p. 1188–1204, https://doi.org/10.1016/j.scitotenv.2018.05.223.

Fryberger, S.G., Al-Sari, A.M., and Clisham, T.J., 1983, Eolian dune, interdune, sand sheet, and siliciclastic sabkha sediments of an offshore prograding sand sea, Dhahran area, Saudi Arabia: AAPG Bulletin, v. 67, no. 2, p. 280–312, https://doi.org/10.1306/03B5ACFF-16D1-11D7-8645000102C1865D.

Gagnon, C.A., Butler, K.L., Gaviria, E., Terrazas, A., Gao, A., Bhattacharya, T., et al., 2023, Paleoclimate controls on lithium enrichment in Great Basin Pliocene–Pleistocene lacustrine clays: Geological Society of America Bulletin, v. 135, p. 3201–3212, https://doi.org/10.1130/B36572.1.

Gillette, D.A., Clayton, R.N., Mayeda, T.K., Jackson, M.L., and Sridhar, K., 1978, Tropospheric aerosols from some major dust storms of the southwestern United States: Journal of Applied Meteorology, v. 17, p. 832–845, https://doi.org/10.1175/1520-0450(1978)017<0832:TAFSMD>2.0.CO;2.

Harrison, S.P., Kohfeld, K.E., Roelandt, C., and Claquin, T., 2001, The role of dust in climate changes today, at the last glacial maximum and in the future: Earth-Science Reviews, v. 54, p. 43-80, https://doi.org/10.1016/S0012-8252(01)00041-1.

Hauck, T.E., 2014, Regional correlation of the Beaverhill Lake Group in the subsurface of Alberta, townships 29 to 113 and ranges 1W4 to 13W6; Alberta Energy Regulator, AER/AGS Open File Report 2014-05, 29 p., https://ags.aer.ca/publications/all-publications/ofr-2014-05.

Hauck, T.E., and Grobe, M., 2020, Upper Elk Point subgroup paleogeography and evaporite distribution with implications for evaporite dissolution, karstification, and carbonate diagenesis in northeastern Alberta: Bulletin of Canadian Petroleum Geology, v. 68, p. 91–122, https://doi.org/10.35767/gscpgbull.68.4.91.

Heier, N.S., and Billings, G.K., 1978, Lithium, *in* Wedepohl, K.H., ed., Handbook of Geochemistry: Springer, p. 3-G-1–3-H-1.

Hitchon, B., Underschultz, J.R., and Bachu, S., 1993, Industrial mineral potential of Alberta formation waters: Alberta Research Council, Alberta Geological Survey, Open File Report 1993-15, 85 p., https://ags.aer.ca/publications/all-publications/ofr-1993-15.

Hofstra, A.H., Todorov, T.I., Mercer, C.N., Adams, D.T., and Marsh, E.E., 2013, Silicate melt inclusion evidence for extreme pre-eruptive enrichment and post-eruptive depletion of lithium in silicic volcanic rocks of the western United States: Implications for the origin of lithium-rich brines: Economic Geology, v. 108, p. 1691–1701, https://doi.org/10.2113/econgeo.108.7.1691.

Hoyer, M., Kummer, N.A., and Merkel, B., 2015, Sorption of lithium on bentonite, kaolin and zeolite: Geosciences, v. 5, p. 127–140, https://doi.org/10.3390/geosciences5020127.

Huff, G.F., 2016, Evolution of Li-enriched oilfield brines in the Devonian carbonates of the south-central Alberta Basin, Canada: Bulletin of Canadian Petroleum Geology, v. 64, p. 438–448, https://doi.org/10.2113/gscpgbull.64.3.438.

Huff, G.F., 2019, Origin and Li-enrichment of selected oilfield brines in the Alberta Basin, Canada: Alberta Geological Survey/Alberta Energy Regulator Open File Report 2019-01, 29 p.

Huh, Y., Chan, L.H., Zhang, L., and Edmond, J.M., 1998, Lithium and its isotopes in major world rivers: Implications for weathering and the oceanic budget: Geochimica et Cosmochimica Acta, v. 62, p. 2039–2051, https://doi.org/10.1016/S0016-7037(98)00126-4.

IEA (International Energy Agency), 2021, Global EV Outlook 2021: International Energy Agency, 101 p., https://www.iea.org/reports/global-ev-outlook-2021 (accessed April 2025).

Jansa, L.F., and Fischbuch, N.R., 1974, Evolution of a Middle and Upper Devonian sequence from a clastic coastal plain–deltaic complex into overlying carbonate reef complexes and banks, Sturgeon-Mitsue area, Alberta: Geological Survey of Canada Bulletin 234, 105 p., https://doi.org/10.4095/103477.

Jensen, G.K.S., Pollard, A., and Rostron, B.J., 2020, Lithium concentration in the Duperow Formation: Preliminary results of geochemical analysis of core samples from two wells in southeastern Saskatchewan, *in* Summary of Investigations 2020, Volume 1: Saskatchewan Geological Survey, Saskatchewan Ministry of Energy and Resources, Miscellaneous Report 2020-4.1, Paper A-2, 8 p. and 1 appendix.

Keith, J.W., 1990, The influence of the Peace River Arch on Beaverhill Lake Sedimentation, *in* O'Connell, S.C., and Bell, J.S., eds., Geology of the Peace River Arch: Bulletin of Canadian Petroleum Geology, v. 38A, p. 55–65, https://doi.org/10.35767/gscpgbull.38a.1.055.

Kharaka, Y.K., and Hanor, J.S., 2003, Deep Fluids in the Continents: I. Sedimentary Basins, *in* Holland, H.D., and Turekian, K.K., eds., Treatise on Geochemistry: Elsevier, v. 5, p. 1–48, https://doi.org/10.1016/B0-08-043751-6/05085-4.

Kirkland, D.W., Denison, R.E., and Dean, W.E., 2000, Parent brine of the Castile evaporites (Upper Permian), Texas and New Mexico: Journal of Sedimentary Research. Section A, Sedimentary Petrology and Processes, v. 70, p. 749–761, https://doi.org/10.1306/2DC40935-0E47-11D7-8643000102C1865D.

Kohfeld, K.E., and Harrison, S.P., 2001, DIRTMAP: The geological record of dust: Earth-Science Reviews, v. 54, p. 81–114, https://doi.org/10.1016/S0012-8252(01)00042-3.

Lazowski, C.N., Kalderon-Asael, B., Asael, D., Arizaleta, M.L., Melnyk, S., Wilson, S., Alessi, D., Planavsky, N.J., Konhauser, K.O., and Gingras, M.K., 2025, Lithium isotopes of the Peace River Arch in the Western Canada Sedimentary Basin: A framework for resolving deep basin lithium sources: Geological Society of America Bulletin, 10.1130/B38102.1.

Lund, J.W., and Toth, A.N., 2021, Direct utilization of geothermal energy 2020 worldwide review: Geothermics, v. 90, https://doi.org/10.1016/j.geothermics.2020.101915.

Maher, B.A., Prospero, J.M., Mackie, D., Gaiero, D., Hesse, P.P., and Balkanski, Y., 2010, Global connections between aeolian dust, climate and ocean biogeochemistry at the present day and at the last glacial maximum: Earth-Science Reviews, v. 99, p. 61–97, https://doi.org/10.1016/j.earscirev.2009.12.001.

Maloney, K.O., and Yoxtheimer, D.A., 2012, Production and disposal of waste materials from gas and oil extraction from the Marcellus Shale play in Pennsylvania: Environmental Practice, v. 14, p. 268–287, https://doi.org/10.1017/S146604661200035X.

Maneta, V., and Baker, D.R., 2019, The potential of lithium in alkali feldspars, quartz and muscovite as a geochemical indicator in the exploration for lithium-rich granitic pegmatites: A case study from the spodumene-rich Moblan pegmatite, Quebec, Canada: Journal of Geochemical Exploration, v. 205, https://doi.org/10.1016/j.gexplo.2019.106336.

McGee, D., Winckler, G., Borunda, A., Serno, S., Anderson, R.F., Recasens, C., et al., 2016, Tracking eolian dust

with helium and thorium: Impacts of grain size and provenance: Geochimica et Cosmochimica Acta, v. 175, p. 47–67, https://doi.org/10.1016/j.gca.2015.11.023.

McMechan, M.E., 1990, Upper Proterozoic to Middle Cambrian history of the Peace River Arch: Evidence from the Rocky Mountains, *in* O'Connell, S.C., and Bell, J.S., eds., Geology of the Peace River Arch: Bulletin of Canadian Petroleum Geology, v. 38A, p. 36–44, https://doi.org/10.35767/gscpgbull.38a.1.036.

McTainsh, G.H., Nickling, W.G., and Lynch, A.W., 1997, Dust deposition and particle size in Mali, West Africa: Catena, v. 29, p. 307–322, https://doi.org/10.1016/S0341-8162(96)00075-6.

Meijer Drees, N.C., 1994, Devonian Elk point group of the western Canada sedimentary basin, *in* Mossop, G.D., and Shetsen, I., compilers, Geological Atlas of the Western Canada Sedimentary Basin: Canadian Society of Petroleum Geologists and Alberta Research Council, v. 4, p. 129–138, https://ags.aer.ca/publications/atlas-western-canada-sedimentary-basin/chapters/chapter-10-devonian-elk-point-group.

Moore, P.F., 1989, The Kaskaskia Sequence: reefs, platforms and foredeeps: The Lower Kaskaskia Sequence—Devonian, *in* Ricketts, B.D., ed., The Western Canadian Sedimentary Basin—A Case History: Calgary, Alberta, Canadian Society of Petroleum Geologists, Special Publication 30, p. 139–164.

Munk, L.A., Boutt, D.F., Hynek, S.A., and Moran, B.J., 2018, Hydrogeochemical fluxes and processes contributing to the formation of lithium-enriched brines in a hyper-arid continental basin: Chemical Geology, v. 493, p. 37–57, https://doi.org/10.1016/j.chemgeo.2018.05.013.

Nabhan, A.I., and Yang, W., 2018, Modern sedimentary facies, depositional environments, and major controlling processes on an arid siliciclastic coast, Al Qahmah, SE Red Sea, Saudi Arabia: Journal of African Earth Sciences, v. 140, p. 9–28, https://doi.org/10.1016/j.jafrearsci.2017.12.014.

Nair, R.R., Hashimi, N.H., and Purnachandra Rao, V., 1982, On the possibility of high-velocity tidal streams as dynamic barriers to longshore sediment transport: Evidence from the continental shelf off the Gulf of Kutch, India: Marine Geology, v. 47, p. 77–86, https://doi.org/10.1016/0025-3227(82)90020-2.

Nickling, W.G., and Neuman, C.K., 2009, Aeolian Sediment Transport, *in* Parsons, A.J., and Abrahams, A.D., eds., Geomorphology of Desert Environments (2nd edition): Dordrecht, Springer, p. 517–555, https://doi.org/10.1007/978-1-4020-5719-9_17.

O'Connell, S.C., Dix, G.R., and Barclay, J.E., 1990, The origin, history, and regional structural development of the Peace River Arch, Western Canada, *in* O'Connell, S.C., and Bell, J.S., eds., Geology of the Peace River Arch: Bulletin of Canadian Petroleum Geology, v. 38A, p. 4–24, https://doi.org/10.35767/gscpgbull.38a.1.004.

Oldale, H.S., and Munday, R.J., 1994, Devonian Beaverhill Lake Group of the Western Canada Sedimentary Basin, *in* Mossop, G.D., and Shetsen, I., compilers, Geological Atlas of the Western Canada Sedimentary Basin: Canadian Society of Petroleum Geologists and Alberta Research Council, p. 149–161, https://ags.aer.ca/publications/atlas-western-canada-sedimentary-basin/chapter-11-devonian-beaverhill-lake-group.

Paton, C., Hellstrom, J., Paul, B., Woodhead, J., and Hergt, J., 2011, Iolite: Freeware for the visualisation and processing of mass spectrometric data: Journal of Analytical Atomic Spectrometry, https://doi.org/10.1039/c1ja10172b.

Pemberton, S.G., MacEachern, J.A., Dashtgard, S.E., Bann, K.L., Gingras, M.K., and Zonneveld, J.P., 2012, Shorefaces: Developments in Sedimentology, v. 64, p. 563–603, https://doi.org/10.1016/B978-0-444-53813-0.00019-8.

Petrash, D.A., Bialik, O.M., Bontognali, T.R.R., Vasconcelos, C., Roberts, J.A., McKenzie, J.A., and Konhauser, K.O., 2017, Microbially catalyzed dolomite formation: From near-surface to burial: Earth-Science Reviews, v. 171, p. 558–582, https://doi.org/10.1016/j.earscirev.2017.06.015.

Pogge von Strandmann, P.A.E., Kasemann, S.A., and Wimpenny, J.B., 2020, Lithium and Lithium Isotopes in Earth's Surface Cycles: Elements, v. 16, p. 253–258, https://doi.org/10.2138/gselements.16.4.253.

Porter, J.W., Price, R.A., and McGrossan, R.G., 1982, The Western Canadian Sedimentary Basin: Philosophical Transactions of the Royal Society A: Mathematical, Physical and Engineering Sciences, v. 305, p. 169–192, https://doi.org/10.1098/rsta.1982.0032.

Pye, K., 1987, Grain Size, Mineralogy and Chemical Composition of Aeolian Dust, *in* Aeolian Dust and Dust Deposits: Academic Press, p. 118–141, https://doi.org/10.1016/B978-0-12-568690-7.50010-7.

Ronov, A.B., Migdisov, A.A., Voskresenskaya, N.T., and Korzina, G.A., 1970, Geochemistry of lithium in the sedimentary cycle: Geochemistry International, v. 7, p. 75–102.

Sanjuan, B., Gourcerol, B., Millot, R., Rettenmaier, D., Jeandel, E., and Rombaut, A., 2022, Lithium-rich geothermal brines in Europe: An up-date about geochemical characteristics and implications for potential Li resources: Geothermics, v. 101, https://doi.org/10.1016/j.geothermics.2022.102385.

Schreiber, B.C., and El Tabakh, M., 2000, Deposition and early alteration of evaporites: Sedimentology, v. 47, p. 215–238, https://doi.org/10.1046/j.1365-3091.2000.00002.x.

Shannon, R.D., 1976, Revised effective ionic radii and systematic studies of interatomic distances in halides and chalcogenides: Acta Crystallographica Section A, v. A32, p. 751–767, http://dx.doi.org/10.1107/S0567739476001551.

Shawa, M.S., 1969, Sedimentary history of the Gilwood Sandstone (Devonian) Utikuma Lake Area, Alberta, Canada: Bulletin of Canadian Petroleum Geology, v. 17, p. 392–409, https://doi.org/10.35767/gscpgbull.17.4.392.

Shearman, D.J., 1978, Evaporites of coastal sabkhas, *in* Dean, W.E., and Schreiber, B.C., eds., Marine Evaporites: Society for Sedimentary Geology (SEPM) Short Course Notes, v. 4, p. 6–42, https://doi.org/10.2110/scn.78.01.0006.

Shinn, E.A., 1983, Tidal flat environment, *in* Scholle, P.A., et al., eds., Carbonate Depositional Environments: American Association of Petroleum Geologists Memoir 33, p. 171–210, https://doi.org/10.1306/M33429C8.

Sikaboyni, L.A., and Rodgers, W.J., 1959, Paleozoic tectonics and sedimentation in the northern half of the west Canadian basin: Journal of the Alberta Society of Petroleum Geologists, v. 7, p. 193–216.

Sinclair, M.R., 1988, Local topographic influence on low-level wind at Scott Base, Antarctica: New Zealand Journal of Geology and Geophysics, v. 31, p. 237–245, https://doi.org/10.1080/00288306.1988.10417772.

Smalley, I.J., and Vita-Finzi, C., 1968, The formation of fine particles in sandy deserts and the nature of 'desert' loess: Journal of Sedimentary Petrology, v. 38, p. 766–774, https://doi.org/10.1306/74d71a69-2b21-11d7-8648000102c1865d.

Stoffynegli, P., and Mackenzie, F.T., 1984, Mass balance of dissolved lithium in the oceans: Geochimica et Cosmochimica Acta, v. 48, p. 859–872, https://doi.org/10.1016/0016-7037(84)90107-8.

Stelck, C.R., 1975, Basement control of Cretaceous sand sequences in Western Canada, *in* Caldwell, W.G.E., ed., The Cretaceous System in the Western Interior of North America: Geological Association of Canada Special Paper 13, p. 474–440.

Stelck, C.R., Burwash, R.A., and Stelck, D.R., 1978, The Vreeland High: A Cordilleran expression of the Peace River Arch: Bulletin of Canadian Petroleum Geology, v. 26, p. 87–104, https://doi.org/10.35767/gscpgbull.26.1.087.

Tanaka, T.Y., and Chiba, M., 2006, A numerical study of the contributions of dust source regions to the global dust budget: Global and Planetary Change, v. 52, p. 88–104, https://doi.org/10.1016/j.gloplacha.2006.02.002.

Taylor, H.L., Kell Duivestein, I.J., Farkas, J., Dietzel, M., and Dosseto, A., 2019, Technical note: Lithium isotopes in dolostone as a palaeo-environmental proxy—An experimental approach: Climate of the Past, v. 15, p. 635–646, https://doi.org/10.5194/cp-15-635-2019.

Teng, F.-Z., McDonough, W.F., Rudnick, R.L., Dalpé, C., Tomascak, P.B., Chappell, B.W., and Gao, S., 2004, Lithium isotopic composition and concentration of the upper continental crust: Geochimica et Cosmochimica Acta, v. 68, p. 4167–4178, https://doi.org/10.1016/j.gca.2004.03.031.

Tesmer, M., Moller, P., Wieland, S., Jahnke, C., Voigt, H., and Pekdeger, A., 2007, Deep reaching fluid flow in the North East German Basin: Origin and processes of groundwater salinisation: Hydrogeology Journal, v. 15, p. 1291–1306, https://doi.org/10.1007/s10040-007-0176-y.

Tomascak, P.B., Magna, T., and Dohmen, R., 2016, Advances in Lithium Isotope Geochemistry: Springer International Publishing, 195 p., https://doi.org/10.1007/978-3-319-01430-2.

Trotter, R., 1989, Sedimentology and depositional setting of the Granite Wash of the Utikuma and Red Earth areas, north-central Alberta [M.Sc. thesis]: Halifax, Nova Scotia, Canada, Dalhousie University, 378 p.

Trotter, R., and Hein, F.J., 1988, Sedimentology and depositional setting of the Granite Wash, northwestern Alberta, *in* James, D.P., and Leckie, D.A., eds., Sequences, Stratigraphy, Sedimentology, Surface and Subsurface: Canadian Society of Petroleum Geologists, Memoir 15, p. 475–484.

Tsoar, H., and Pye, K., 1987, Dust transport and the question of desert loess formation: Sedimentology, v. 34, p. 139–153, https://doi.org/10.1111/j.1365-3091.1987.tb00566.x.

USGS (U.S. Geological Survey), 2023, Mineral commodity summaries 2023: U.S. Geological Survey, 210 p., https://doi.org/10.3133/mcs2023.

Vasconcelos, C., and McKenzie, J.A., 1997, Microbial mediation of modern dolomite precipitation and diagenesis under anoxic conditions (Lagoa Vermelha, Rio de Janeiro, Brazil): Journal of Sedimentary Research, v. 67, p. 378–390, https://doi.org/10.1306/D4268577-2B26-11D7-8648000102C1865D.

Vera, M.L., Torres, W.R., Galli, C.I., Chagnes, A., and Flexer, V., 2023, Environmental impact of direct lithium extraction from brines: Nature Reviews Earth & Environment, v. 4, p. 149–165, https://doi.org/10.1038/s43017-022-00387-5.

Warren, J.K., 2016, Evaporites: A Geological Compendium (2nd edition): Berlin, Springer International Publishing, 1813 p, https://doi.org/10.1007/978-3-319-13512-0.

Warren, J.K., and Kendall, C.G., 1985, Comparison of sequences formed in marine sabkha (subaerial) and salina (subaqueous) settings—Modern and ancient: American Association of Petroleum Geologists Bulletin, v. 69, p. 1013–1023, https://doi.org/10.1306/AD462B46-16F7-11D7-8645000102C1865D.

Whalley, W.B., and Smith, B.J., 1981, Mineral content of Harmattan dust from northern Nigeria examined by scanning electron microscopy: Journal of Arid Environments, v. 4, p. 21–29, https://doi.org/10.1016/S0140-1963(18)31590-8.

Wilson, T.P., and Long, D.T., 1993, Geochemistry and isotope chemistry of Michigan Basin brines: Devonian formations: Applied Geochemistry, v. 8, p. 81–100, https://doi.org/10.1016/0883-2927(93)90058-O.

Witzke, B.J., and Heckel, P.H., 1988, Paleoclimatic indicators and inferred Devonia paleolatitudes of Euramerica, *in* McMillan, N.J., Embry, A.F., and Glass, D.J., eds., Devonian of the World: Canadian Society of Petroleum Geologists, Second International Symposium on the Devonian System, v. 1, p. 49–68.

Zheng, M., and Liu, W., 1987, A new Li-mineral—Zabuyelite: Acta Mineralogica Sinica, v. 7, p. 221–226.

Science Editor: Troy Rasbury
Associate Editor: Rajat Mazumder

Manuscript Received 1 November 2024
Revised Manuscript Received 6 March 2025
Manuscript Accepted 25 April 2025